



HAL
open science

Revisiting the Malvinas Current upper circulation and water masses using a highresolution ocean reanalysis

Camila Artana, Christine Provost, Léa Poli, Ramiro Ferrari, Jean-Michel Lellouche

► **To cite this version:**

Camila Artana, Christine Provost, Léa Poli, Ramiro Ferrari, Jean-Michel Lellouche. Revisiting the Malvinas Current upper circulation and water masses using a highresolution ocean reanalysis. *Journal of Geophysical Research. Oceans*, 2021, 126 (6), 10.1029/2021JC017271 . hal-03247496

HAL Id: hal-03247496

<https://hal.sorbonne-universite.fr/hal-03247496>

Submitted on 3 Jun 2021

HAL is a multi-disciplinary open access archive for the deposit and dissemination of scientific research documents, whether they are published or not. The documents may come from teaching and research institutions in France or abroad, or from public or private research centers.

L'archive ouverte pluridisciplinaire **HAL**, est destinée au dépôt et à la diffusion de documents scientifiques de niveau recherche, publiés ou non, émanant des établissements d'enseignement et de recherche français ou étrangers, des laboratoires publics ou privés.

32 **Abstract:**

33

34 We use 25 years of a high-resolution ocean reanalysis ($1/12^\circ$) to revisit the Malvinas Current
35 (MC) from the South (Drake Passage) to the North (Brazil-Malvinas Confluence) from the
36 synoptic to interannual time scales. The Malvinas Plateau is home to active eddy mixing, eddy
37 dissipation and deep winter mixed layers occasionally reaching 600 m depth. The MC is
38 organized in two jets which merge around 44°S as the continental slope steepens. The upper
39 900 m transport mean decreases from 40 Sv at 51°S to 35 Sv at 41°S indicating offshore leakage
40 along the MC path. The MC plays a minor role in the velocity variations observed at the
41 Confluence at seasonal and interannual scales; those are driven by changes in the intensity of
42 the Brazil Current over the slope ($34\text{-}36^\circ\text{S}$).

43 Computing MC transport time series at different latitudes requires care because the section
44 eastern limits are embedded in an energetic region. Transport time series were produced at
45 selected latitudes using different criteria and showed common features. They show little
46 seasonality (relative seasonal standard deviation of 2%) and no significant trend. The MC is a
47 steady current: the relative standard deviation is on the order of 10% increasing to 20% near
48 and on the Malvinas Plateau and near the Confluence. In contrast, velocity trends are large in
49 the Brazil Current with the overshoot migrating southward. The associated increase in
50 mesoscale activity south of 44°S in the Argentine Basin might contribute to blocking events
51 occasionally reducing the MC transport.

52

53

54

55

56

57

58 **Plain language summary**

59

60 The Malvinas Current (MC) is a branch of the Antarctic Circumpolar Current and flows
61 northward along the Patagonian slope. We revisit the Malvinas Current upper circulation and
62 water masses using a high-resolution ocean reanalysis from 1993 to 2017. The MC is a strong
63 and rather steady current with little seasonality and no significant trend. The mean MC volume
64 transport reduces from south to north by about 14%, indicating an offshore leakage along its
65 path. The upper 500 m MC waters underwent a freshening of 0.1 psu/decade.

66

67

68

69

70

71

72

73

74

75

76

77

78

79

80

81

82

83

84

85

86

87

88

89

90

91

92

93

94

95 **1. Introduction**

96 The Malvinas Current (MC), a major western boundary current of the South Atlantic, is the
97 northernmost meander of the northern branch of the Antarctic Circumpolar Current (ACC), the
98 Subantarctic Front (SAF). The North Scotia Ridge in Drake Passage (Figure 1 a) acts as a
99 barrier to the ACC fronts forcing the SAF and Polar Front (PF) branches to deviate to the north.
100 The two SAF branches (SAF-N and SAF-M) cross the North Scotia Ridge west (600 m) and
101 east (2000 m) of Burdwood Bank (WBB and EBB respectively), while the two northern
102 branches of the PF (PF-M and PF-N) proceed through Shag Rocks Passage (3200 m, SRP)
103 (Figure 1a). Subsequently, the SAF branches cross the shallow Malvinas Plateau (<3000 m)
104 and continue their path northward forming the Malvinas Current (MC), while the PF follows
105 an eastward path along the Malvinas Escarpment (Figure 1a). The MC is an equivalent-
106 barotropic current that flows along the Patagonian continental slope with surface velocities of
107 the order of 60 cm/s (Figure 1b). Observations suggest that the MC is organized in two narrow
108 jets at 45°S (Piola et al., 2013, Frey et al., 2021). Poli et al. (2020) showed that shelf break
109 trapped waves modulate the intensity of the inner jet -SAF-N branch- while slow waves
110 propagating from the Malvinas Escarpment and the Drake Passage modify velocities in the
111 main jet -SAF-M branch- (Figure 2a). The Malvinas Current is concentrated in a narrow single
112 jet at 41°S and encounters the Brazil Current (BC) at 38°S. Then part of the BC, referred to as
113 the overshoot of the BC, flows southward and returns to the northeast at about 45°S while the
114 MC splits in two branches: the inner branch keeps flowing northward sinking below the BC
115 while the outer branch describes a sharp cyclonic loop and returns southward (Provost et al.,
116 1995; Artana et al., 2019a). The southward return flow is referred to as the Malvinas Return
117 Flow (Peterson and Whitworth, 1989). The region of the confluence is known as the Brazil
118 Malvinas Confluence and is associated with lateral temperature gradients as high as 1°C per

119 100 m (Gordon and Greengrove, 1986; Barré et al., 2006) and large meso and submesoscale
120 eddies and filaments.

121 Interestingly, although the MC presents moderate Eddy Kinetic Energy (EKE) values ($\sqrt{\text{EKE}}$
122 of 15 cm/s), it connects two of the most energetic oceanic regions: the Drake Passage ($\sqrt{\text{EKE}}$
123 of 30 cm/s) and the Brazil Malvinas Confluence ($\sqrt{\text{EKE}}$ of 45 cm/s, Figure 1c). Some of the
124 Drake Passage EKE leaks across the North Scotia Ridge through the EBB and SRP and reduces
125 over the Malvinas Plateau through dissipation and mixing (Artana et al., 2016, Figure 2a). As
126 a result, $\sqrt{\text{EKE}}$ values over the Malvinas Plateau are in the order of 15 cm/s (Figure 1c). At the
127 exit of the Malvinas Plateau, the MC is particularly exposed to mesoscale activity propagating
128 westward along the Malvinas Escarpment. Around once a year the MC is cut from the ACC
129 due to anticyclonic anomalies from the deep Argentine Basin (red in Figure 2b, Artana et al.,
130 2016 and Artana et al., 2018a). These blocking events are short-lived (from 10 to 35 days) and
131 the MC downstream does not collapse rather becomes the western boundary of a recirculating
132 cyclonic cell. Occasionally, the PF-N meanders north of the Malvinas Plateau and waters from
133 the South of the Polar Front (PF) are injected into the MC as pulses or feeding events (blue in
134 Figure 2b, Artana et al., 2018c). Polar waters accumulate in the recirculation region between
135 the MC and the Malvinas Return Flow. Low frequency variations in the water characteristics
136 of the recirculation region are consistent with changes in the recurrence of feeding events.

137 The MC is the unique current in the southern hemisphere that carries Subantarctic Surface
138 Water and Antarctic Intermediate Waters to latitudes as low as 38°S. These cold and nutrient
139 rich waters are key for the development of rich ecosystems along the Patagonian shelf which
140 sustain one of the largest fisheries of the world (Romero et al., 2006; Valla and Piola, 2015).
141 The modification of water properties along the MC path is poorly understood and an evaluation
142 of the MC transport over its latitudinal range is missing. To the date, the only volume transport

143 time series of the MC have been produced at 41°S near the Brazil Malvinas Confluence where
144 mooring data were gathered at different periods (Vivier and Provost, 1999a; Spadone and
145 Provost, 2009; Paniagua et al., 2018). The mooring data were combined with satellite altimetry
146 data to produce a 25 year-long transport time series in the upper 1500 m (Artana et al., 2018a).
147 Maxima and minima of the MC transport at 41°S were not associated with variations of the
148 ACC, rather with eddies coming from the Argentine Basin: maxima were associated with
149 cyclonic eddies detached from the Polar Front (in blue in Figure 2c) and minima with large
150 anticyclonic anomalies from the Brazil Current (in red in Figure 2c).

151 Here we revisit the Malvinas Current from its southern part to its northernmost tip from
152 synoptic to interannual time scales using 25 years of the high-resolution Mercator Ocean
153 reanalysis GLORYS12. This reanalysis has shown skills in reproducing the hydrography and
154 circulation of the Argentine Basin in the upper layers and proved to be a most valuable tool to
155 study the MC in this region where in situ observations are rather scarce (Artana et al., 2018b,
156 2018c, 2019a; Poli et al., 2020). We aim at assessing the MC transport at different latitudes
157 and at documenting modification of MC water properties. We focus on the upper circulation
158 and upper water masses of the MC all along its path. After a presentation of the reanalysis and
159 its evaluation (section 2), we investigate the velocity structure along the continental slope and
160 produce volume transport time series in the upper 900 m at different latitudes (section 3).
161 Modifications of the Subantarctic Surface Water and Antarctic Intermediate Waters are
162 examined in section 4 and their volume transport evolutions in section 5. Results are
163 summarized in section 6.

164

165

166

167 **2. Mercator Ocean reanalysis**

168 **2.1 Description of the GLORYS12 reanalysis**

169 We use daily means of 25 years (1993–2017) of high-resolution (1/12°) global Mercator Ocean
170 reanalysis (hereafter, GLORYS12) from Copernicus Marine Environment Monitoring Service
171 (CMEMS, <http://marine.copernicus.eu/>). GLORYS12 is based on the current real-time global
172 high-resolution forecasting CMEMS system PSY4V3 (Lellouche et al., 2018). Compared to
173 PSY4V3, GLORYS12 reanalysis uses the reprocessed atmospheric forcing coming from the
174 global atmospheric reanalysis ERA-Interim and benefits from a few changes in the system
175 settings about observation errors. The model has 50 vertical levels with 22 levels in the upper
176 100 m leading to a vertical resolution of 1 m in the upper levels and 450 m at 5000 m depth.
177 The physical component of the model is the Nucleus for European Modeling of the Ocean
178 platform (NEMO). The model assimilates observations using a reduced-order Kalman filter
179 with a 3-D multivariate modal decomposition of the background error and a 7-day assimilation
180 cycle (Lellouche et al., 2013). Along-track satellite altimetric data from CMEMS (Pujol et al.,
181 2016), satellite sea surface temperature from NOAA, sea-ice concentration, and in situ
182 temperature and salinity vertical profiles from the latest CORA in situ databases (Cabanes et
183 al., 2013; Szekeley et al., 2016) are jointly assimilated. A 3D-VAR scheme provides an
184 additional 3-D correction for the slowly evolving large-scale biases in temperature and salinity
185 when enough observations are available (Lellouche et al., 2018).

186 **2.2 GLORYS12 evaluation in the Southwestern Atlantic and Drake Passage**

187 In a previous work, Artana et al. (2018b) evaluated the performance of PSY4V3 in the
188 Southwestern Atlantic Ocean. Ten years (2007–2016) of model outputs were compared to
189 assimilated satellite and Argo float data and to independent in situ data that were not
190 assimilated. The comparison showed that the PSY4V3 system correctly reproduces the general

191 circulation and the complex hydrographic features of the Southwestern Atlantic Ocean upper
192 layers. The authors found an excellent agreement between model and satellite sea surface
193 height (Artana et al., 2018c). In a subsequent work general agreement between GLORYS12
194 and PSY4V3 was found, and comparisons with observations showed that GLORYS12 is closer
195 to the data than PSY4V3 in the region of interest (Artana, et al., 2018c).

196 An extensive evaluation of GLORYS12 velocities was also performed at Drake Passage
197 (Artana et al., 2019b). GLORYS12 velocities compared well with independent current meter
198 data in the water column and 50 m above the seafloor. The GLORYS12 total ACC volume
199 transport has a mean of 155 (3 Sv being the uncertainty on the mean) and a standard deviation
200 (std) of 6.7 Sv over 25 years (Artana et al., 2019b).

201 Here we focus on the upper MC as GLORYS12 performance was only evaluated in the upper
202 layers of the Southwestern Atlantic Ocean. We tentatively examined the stream function of the
203 mean volume transport between the surface and the bottom in the Southwestern Atlantic Ocean:
204 the total MC transport decreases from 75 Sv at 51°S to 55 Sv at 47°S and 50 Sv at 44.7 and
205 41°S. These values are consistent with the few total volume transport estimates derived from
206 in situ data (Peterson, 1992; Saunders and King, 1995; Maamaatuaiahutapu et al., 1998; Colin
207 de Verdière and Ollitrault, 2016) (see supplementary material S1).

208 **3. The MC upper circulation**

209 **3.1 Surface velocity: Mean and variations**

210 The MC mean surface velocity structure evolves with the continental slope geometry (Figure
211 1b, Figure 3). At 51°S, over the Malvinas Plateau, the slope is gentle (8 m/km), the mean MC
212 organized in two rather wide jets (150 km and 200 km, purple in Figure 3b) centered on local
213 gradient bathymetry maxima (10 m/km) located on the 400 and 1500 m isobaths. The inner (20
214 cm/s) and offshore jets (25 cm/s) are associated with the SAF-N and the SAF-M respectively.
215 Further east, a smaller jet (8 cm/s) above the 2000 m isobath corresponds to the northern branch

216 of the PF. Further north, as the slope steepens, the jets narrow, intensify and then merge around
217 44°S (Figure 1b). Between 51°S and 46°S, the offshore jet is located above the 1500/1400 m
218 isobath while the inshore jet follows the shelf break which varies between 300 and 500 m
219 (green and orange sections in Figure 3). The mean surface velocity of the offshore jet increases
220 towards the north ranging from 25 cm/s at 51°S to 40 cm/s at 47°S. In general, the mean surface
221 velocities of the offshore jet are twice as large as those of the inshore jet. However, at 44.7°S
222 where the MC transitions to a single jet regime as the slope steepens (30 m/km), the two jets
223 merge and the largest surface velocities (58 cm/s) are found above 200 m (blue section in Figure
224 3). This is consistent with mean surface velocities derived from the mean dynamic
225 topography from Mulet et al. (2020) (see supplementary material S2) and a month-long record
226 of ADCP observations above the 200 m isobath at 44.7°S which documented velocities as large
227 as 68 cm/s at 20 m depth (Saraceno et al., 2020).

228 Overall, the MC is a rather stable current with surface velocities presenting relatively
229 homogeneous and small stds (10 cm/s, Figures 1c and 3b). Std of the surface velocity is larger
230 in the outer part of the sections, in particular at 51°S, 59°W and 41°S (~15 cm/s, Figure 3d),
231 which are under the influence of offshore perturbations (Figure 1c). The impact of the offshore
232 mesoscale activity on the MC surface velocities is illustrated in a synoptic situation in the
233 supplementary material S3.

234 Surface velocities do not change in the MC at seasonal time scale while they increase by 15
235 cm/s in summer at the BC and Brazil Malvinas Confluence (Figure 4a-b). The overshoot is
236 located 3 degrees further south in winter (44°S-54°W) than in summer. The velocities in the
237 overshoot are larger in winter (+15 cm/s) suggesting that the BC summer intensification
238 advects into a winter intensification of the overshoot. The SAF remains at a similar position
239 regardless of the season and the Subtropical Front pivots over a point located at 38°S over the
240 slope (1000 m isobath) as observed in Saraceno et al. (2005). In relation with the overshoot

241 seasonal displacement, the offshore EKE shows large values further south in winter (not
242 shown).

243 Surface velocity trends over the 25 years are relatively small, although significant in the MC,
244 with a weakening (-2 cm/s/decade) in the inshore part of the MC and a strengthening in the
245 offshore part (2 cm/s/decade) possibly indicating an offshore displacement of 20 km (Figure
246 4c). The surface velocity trend also suggests a small shift in the position of the northern branch
247 Polar Front over the Malvinas Plateau of 60 km westward. Interestingly the EKE surface trends
248 are positive over EBB and the eastward flank of SRP ($50 \text{ cm}^2/\text{s}^2/\text{decade}$) suggesting an increase
249 of the EKE leakage towards the Malvinas Plateau.

250 Surface velocity trends over the slope are large around 38°S (10 cm/s/decade) and reflect the
251 southward displacement of the confluence associated with an intensification of the southward
252 flow of the BC as observed in Artana et al. (2019a). The large cyclonic structure centered at
253 55°W - 43°S in the surface velocity trend indicates a southward displacement of the BC
254 overshoot with an intensification of the surface velocities south of 44°S (Figure 4c). As a result,
255 the EKE trends are positive and large ($150 \text{ cm}^2/\text{s}^2/\text{decade}$) in the southward part of the
256 Argentine Deep Basin (Figure 4d).

257 The MC presents a barotropic equivalent structure (Vivier and Provost, 1999b) and the features
258 at depth are consistent with those observed at the surface as shown in the stream function of
259 the mean volume transport in the upper 900 m (Figure 5).

260 **3.2 Volume transport in the upper 900 m**

261 The MC mean transport in the upper 900 m at 44.7°S is about 37 Sv with a contribution of 3
262 Sv from WBB, 23 Sv from EBB, and 11 Sv from SRP (Figure 5a, transport streamlines every
263 5 Sv). About two thirds of the full SRP transport follow the PF, turn eastward and do not reach
264 44.7°S . Near the Confluence, at 41°S the mean MC transport (35 Sv) is larger than the BC

265 mean transport (20 Sv at 36°S). The upper 900 m transport does not change with seasons over
266 the MC while it increases by 10 Sv over the BC in summer and by 5 Sv over the overshoot in
267 winter (Figure 5b-c) in agreement with the surface velocity seasonality discussed in section
268 3.1. The transport seasonal behavior is robust: seasonal averages computed over different years
269 yield similar results (not shown).

270 The MC transport does exhibit variations at interannual scale. As an example, we show the
271 mean transports in 2015 and 2003 which correspond, respectively, to small (30 Sv) and large
272 (40 Sv) values at 41°S (Artana et al., 2018a and 2019a). Interestingly the MC transport
273 upstream, between 48 and 42°S, is 5 Sv larger than the mean in 2015 and similar to the mean
274 (35 Sv) in 2003 (Figure 5d-e). This example illustrates that the transport variations at 41°S do
275 not reflect upstream MC transport changes rather local perturbations near the Confluence (as
276 schematized in Figure 2c). Indeed, anticyclones from the overshoot reduced the transport by 5
277 Sv at 41°S in 2015, while in 2003 cyclones from the south advected offshore over the 4000 m
278 isobath locally reinforce the MC transport when they reached 41°S (Figure 5d-e; Artana et al.,
279 2018c). The return flow of the Malvinas Current shows different behaviors in 2003 and 2015.
280 While in 2003 the Malvinas Return Flow flows straightforward south towards the Malvinas
281 Escarpment, in 2015 part of the Malvinas Return Flow turns northwestward following the BC
282 overshoot.

283 MC volume transport time series in the upper 900 m were estimated at five latitudes in different
284 ways to account for the difficulty in defining an eastern boundary to the sections. Indeed, if the
285 section western boundary is straightforward, taken here as the 100 m isobath, the eastern limit
286 is open and lies in an energetic environment. Sensitivity tests to the length of the sections were
287 performed (extending and reducing the section length by 50 km). Volume transports time series
288 were estimated considering positive (T+) and both sign velocities (T+-). The times series are

289 presented in supplementary S4 and their statistics in Table 1. From now on we only examine
290 (T+) time series as (T+) and (T+-) are highly correlated (the lowest correlation of 0.62 observed
291 at 44.7°S results from the recurrent southward flow of the Malvinas Return Flow impinging on
292 the eastern part of the section) and (T+) means are closer to the mean values shown in Figure
293 5a (being 6 to 10 Sv larger than (T+-)). As expected, the std is largest (>8 Sv) at 41°S, 59°W
294 and 51°S sections where the offshore side of the sections reaches a large EKE region (Table 1,
295 Figure 1c). Correlations between transport time series from different latitudes are significant
296 (above the 99% confidence level) although relatively small because of the local mesoscale
297 activity on the eastern boundary of each section (Table 2). The upper 900 m transport time
298 series at EBB and SRP are not correlated with the transport of the sections located further north.
299 This is consistent with Artana et al. (2016) who showed that an important part of the mesoscale
300 activity coming from Drake Passage is damped out over the Malvinas Plateau (Figure 2a). The
301 range of variations at synoptic scale is of the order of 30 Sv. The transport varies over a
302 relatively small range at seasonal scale (<5 Sv on average) in contrast to the larger interannual
303 variations (range larger than 10 Sv on average).

304 The MC carries several water masses that we examine focusing on their temporal and spatial
305 distribution, their modification and long-term changes.

306 **4. Water masses in the MC**

307 Following Maamaatuaiahutapu et al. (1994), several water masses are identified at 51°S
308 (Figure 6a-c). The mean temperature and salinity of the upper 100 m (4.8°C and 34.05 psu)
309 correspond to the light Subantarctic Surface Water (SASW; $\sigma_\theta < 27.00 \text{ kg/m}^3$). Below, three
310 varieties of AAIW can be distinguished (Provost et al., 1995): the light upper AAIW (AAIW-
311 U) ($27.00 < \sigma_\theta < 27.14 \text{ kg/m}^3$), a central AAIW (AAIW-C, $27.14 < \sigma_\theta < 27.29 \text{ kg/m}^3$), and a
312 lower AAIW (AAIW-L, $27.29 < \sigma_\theta < 27.35 \text{ kg/m}^3$). The AAIW-U and AAIW-C are classified

313 as Subantarctic Mode Water (SAMW, Provost et al., 1995). Underneath the AAIW, Upper
314 Circumpolar Deep Waters (UCDW) correspond to potential density between 27.35 and 27.73
315 kg/m^3 . The std in salinity and density show a local maximum at the interface between the
316 AAIW and UCDW at depth of 34.25 and 34.32 psu isohaline and 27.3 and 27.35 kg/m^3
317 isopycnals (Figure 6f-g). The depth of AAIW-UCDW interface varies over a range of 200 m.
318 In contrast, the std of potential temperature decreases monotonically with depth as AAIW and
319 UCDW have similar temperatures (between 2.7°C and 2.5°C) (Figure 6a). The range in Θ/S
320 delimiting the AAIW-UCDW interface is shaded in Figure 6i.

321 **4.1 Spatial distribution of the SASW and AAIW layer (Malvinas Upper Waters)**

322 We focused on SASW and AAIW called hereafter MUW (for Malvinas Upper Waters). Θ/S
323 criteria (in the range of the shaded area in Figure 6i) were used to define the lower boundary
324 of the MUW layer. On average, the MUW occupy a thick layer (>800 m) reaching the surface
325 along the Patagonian slope and Malvinas Plateau, and, a thinner layer isolated from the surface
326 offshore (Figure 7a and b). The thin layer in the subtropical gyre (<300 m) is found at depth
327 below 800 m and corresponds to eroded AAIW with Indian Ocean influence recirculating
328 southward (Gordon et al., 1992; Maamaatuaiahutapu et al., 1998).

329 We computed the presence probability of the MUW in the upper 900 m over the 25 years
330 (Figure 7c): 100% means that these waters occupy the upper 900 m all the time. The MUW are
331 mostly common (>90% of occurrences) in the upper 900 m at EBB and all along the Patagonian
332 continental slope south of 38°S (Figure 7c). The MUW water flow occurs primarily in a narrow
333 band closely following the continental slope.

334

335

336 **4.2 Modification through winter convection**

337 We investigate MUW modification through deep mixed layer formation. Two mixed-layer
338 depth (MLD) definitions, one based on potential density and the other on turbocline (de Boyer
339 Montegut et al., 2004), provided similar results. Large winter MLDs occur over the western
340 portion of the Malvinas Plateau reaching 300 m in August on average over 25 years (Figure
341 8a) and maximum values of 600 m (Figure 8b). Winter mixing convection contributes to the
342 regular outcropping of 27 kg/m^3 and 27.1 kg/m^3 isopycnals over the Malvinas Plateau (Figure
343 8c). During some winters, water as dense as 27.10 kg/m^3 is found at the surface as north as
344 44°S . The maps of potential density maxima at the surface from GLORYS12 are consistent
345 with maps of 27.10 and 27.20 kg/m^3 isopycnal depths constructed from winter data collected
346 in 1980 (Piola and Gordon, 1989).

347 The winter MLD and surface potential density over the Malvinas Plateau undergo large
348 interannual variations as illustrated at 51°S over the 1500 m isobath (Figure 8e). Although the
349 MLD time series mimics the surface potential density time series, the deepest MLD do not
350 always correspond to the largest surface density values as other processes contribute to modify
351 density in winter (e.g., eddy mixing, lateral fluxes). The potential density and MLD time series
352 suggest a low frequency modulation (e.g. deep MLD observed in 95-97, 00-02 and 11-12)
353 (Figure 8e). August 2011 registered the deepest (500 m) MLD of the time series. Contrasted
354 synoptic situations in January and August 2011 (Figure 9) along section 51°S illustrate
355 processes at stake on the Plateau and are compared to the mean (Figure 6).

356 **4.3 Modification of water properties on the Malvinas Plateau**

357 Synoptic Sea Surface Height maps (Figure 9a and f) show an exacerbated mesoscale field
358 compared to the rather smoothed mean field (Figure 6j). The Frontal Zone region (between the
359 SAF-M and PF-N), which corresponds to the large deep reaching velocity std values (Figure

360 6h), is filled with energetic eddies and meanders leading to active stirring of properties. Indeed,
361 the temperature and salinity fields in the Frontal Zone are drastically different from the smooth
362 means (Figure 9b, c, g and h to be compared with 6a and b) with intrusions of cold and fresh
363 water in the upper 500 m. For example, the 34.05 psu isohaline that is confined near the surface
364 in the mean field deepens down to 450 m (km 450 in Figure 9 b) while the 3°C isotherm rises
365 by 700 m in January (between km 200 and 400 in Figure 9c), which is consistent with the large
366 std values (Figure 6e and f). The spectacular change in the Θ -S diagram between January and
367 August (Figure 9e and j) reflects the winter convection that reaches the 27.1 kg/m³ σ_θ -horizon
368 ventilating the AAIW-U. Indeed, the MLD changes from ten meters in January (strong summer
369 thermocline) to over 500 m in August in the SAF region.

370 Selected Θ -S profiles in January show two changes in the slope of the Θ -S distribution between
371 the 27.0 and 27.1 kg/m³ isopycnals (e.g., green profile in Figure 9e). They illustrate the lateral
372 exchanges in the Frontal Zone where the cool and fresh waters from the PF encounter the
373 warmer and salty waters from the west of the SAF. In August the change in slope in the Θ -S
374 distribution located on the 27.15 kg/m³ σ_θ -horizon is associated to a profile within a meander
375 of the PF (red profile in Figure 9j). These polar waters will eventually contribute to the
376 freshening and cooling in the Frontal Zone in the upper 500 m and the change in slope will
377 migrate to a lighter horizon (as seen in January).

378 **5. MUW volume transports**

379 MUW volume transports at each time step were estimated using Θ /S criteria in the range
380 defined in Figure 6i ($\Theta > \Theta_0$ and $33.9 < S < S_0$ with Θ_0 varying between 2.5 and 2.7°C and S_0
381 between 34.25 and 34.32). Sensitivities to the temperature and salinity criteria, to the length of
382 the sections were carefully examined using different Θ /S thresholds, extending sections
383 towards the east and, considering positive only (T+) and all velocities (T+-) (see supplementary

384 material S6). We also checked the impact of trends in water properties. Indeed, over the slope
385 south of 40°S and Malvinas Plateau, rather large freshening trends (with values 0.1, 0.08 and
386 0.04 psu/decade at 50, 155 and 541 m respectively) lead to density decreases of about 0.05
387 kg/m³/decade while temperature trends are small (supplementary material S6). However, the
388 34.25/34.32 psu isohalines remained roughly at the same place (slightly deepening and larger
389 vertical salinity gradient) and therefore the bottom limit of the MUW did not change much.
390 The results were robust, yielded highly correlated transport times series ($r > 0.7$), means within
391 a range of 6 Sv and stds within a range of 3 Sv. The relative uncertainty of the mean transport
392 was of the order of 16% for (T+-) (means within a 6 Sv range) and reduced to 5% (means
393 within a 1.5 Sv range) for (T+). Hereafter we discuss MUW transport computed from positive
394 velocities in the layer defined by $\Theta > 2.5^{\circ}\text{C}$ and $33.9 < S < 34.25$ psu. The MUW transport time
395 series (T+) and (T+-) are shown in supplementary material (S5) and their statistics summarized
396 in Table 3.

397 **5.1 The Malvinas Upper Water transport**

398 The northward MUW transport means decrease towards the north from 31 Sv at 51°S to 27 Sv
399 at 41°S indicating offshore leakage and mixing (Figure 10 a). The transport std decreases from
400 4.6 Sv at 51°S to 3.4 Sv at 44°S and shows larger values at 41°S near the Confluence (5 Sv)
401 and at 59°W (5 Sv) near the blocking region (Figure 2b) where the offshore side of the sections
402 reaches a large EKE region (Figure 1c). MUW transport time series (daily resolution) from
403 different latitudes are significantly correlated and maximum correlations between sections are
404 obtained at small lags (<5 days) (Table 2). The smallest correlations are found with the 41°S,
405 59°W and 51°S sections which receive perturbations from the Confluence, from
406 blocking/feeding events and, from Drake Passage, respectively (Figure 2) locally affecting the

407 transport. Correlations between MUW transport time series at different latitudes are larger
408 (>0.2) than those obtained for the upper 900 m transport time series (Table 2).

409 The five MUW transport time series do not exhibit much variation at the seasonal time scale
410 (small increase of 2 Sv in winter in all sections, Figure 10 b) and no long-term trend. Annual
411 means vary over a range of about 6 Sv. The annual means show a decrease in 2004 in the five
412 sections (from 3 to 7 Sv). The 2004 transport minimum is examined below.

413 **5.2 Comparison to upper 900 m transport**

414 We compared the MUW transport (integrated in the layer defined by $\Theta > 2.5^{\circ}\text{C}$ and
415 $33.9 < S < 34.25$ psu) at 44°S and 47°S to the MC transport without water mass distinction,
416 integrated in the first 900 m (Figure 11a and b). The std and mean transport considering the
417 first 900 m is larger than the MUW transport (mean of 37 and 42 Sv and stds of 4 and 4.8 Sv
418 at 44.7°S and 47°S respectively).

419 The MUW and the 900 m volume transport time series are correlated ($r > 0.8$ above the 99%
420 confidence level). However, at specific events they show an opposite behavior with the 900 m
421 transport experiencing an increase and the MUW transport a drastic decrease (e.g., year 1995,
422 2004 end of 2011 in Figure 11a and b). The dates of large difference correspond to feedings
423 events of the MC when Polar waters are supplied to the offshore side of the MC as the PF-N
424 meanders northward (Figure 2b, Figure 11c and d, Artana et al., 2018c). Indeed, polar waters
425 are not considered in the MUW transport computation leading to a decrease in the MUW
426 transport while the PF-N cyclonic meander of the PF-N tends to accelerate the offshore MC
427 flow leading to an increase in the 900 m transport. The transport differences are larger during
428 years 93-97 and 04-17 in agreement with increased occurrence of feeding events during these
429 periods (Figure 11c and d). In contrast, transport differences reduce during blocking events

430 (Figure 2b) as the anticyclonic anomalies obstructing the MC flow at 49°S carry warm and
431 salty waters that are not included in the MUW transport computation (Figure 11c and d).

432 Year 2004 stands out with prolonged feeding events and two blocking events in March and
433 October (Figure 11 c and d). The feeding and blocking events lasted 30 days and 40 days and
434 were associated with density anomalies of +0.08 kg/m³ and -0.13 kg/m³, respectively. This year
435 corresponds to a notable decrease in the MUW annual mean transports at all latitudes (Figure
436 10c) while the 900 m annual mean transport is 0.5 Sv larger than the mean (not shown). In year
437 2004 the South Atlantic Subtropical High was located to the southwest of its mean location
438 (Figure 12a) and a large southward intrusion of salty and warm subtropical waters into the
439 Argentine Basin occurred (Figure 12b). As a result, salinity increased by more than 0.2 psu at
440 the surface and 0.1 psu at 541 m in the western Argentine Basin (Figure 12 c and e). In
441 particular, waters saltier than 34.25 psu reached the offshore side of the northern sections (41°S,
442 44°S and 47°S) on several occasions (Figure 12d) and, in March and October generated two
443 blocking events on the 59°W section (not shown).

444 All over the Patagonian slope waters were 0.1 psu fresher at the surface and 0.1 saltier at 541
445 m as a result of the prolonged feeding events (Figure 12 b-e). The salty (>34.25 psu) waters
446 from the blocking and feeding (delimited with red in Figure 12b and d) events are excluded
447 from the computation of the MUW transport, explaining the decrease in the annual means in
448 2004 (Figure 10c).

449 Interestingly, the feeding events contributed to increase the stratification in the southern part
450 of the MC thereby probably leading to the minimum observed in the winter MLD in 2004
451 (Figure 8e).

452

453

454 **6. Summary and discussion:**

455 This work builds upon previous works that assessed GLORYS12 skills in the upper layer in
456 the Southwestern Atlantic Ocean. We used 25 years of GLORYS12 ocean reanalysis to revisit
457 the upper Malvinas Current along its path from Drake Passage to the Brazil-Malvinas
458 Confluence from synoptic to interannual time scales. In the upper 900 m, the MC carries
459 Subantarctic Surface Waters and Antarctic Intermediate Water (we called them, Malvinas
460 Upper Waters, MUW) and some Upper Circumpolar Deep Waters.

461 The MC is a rather steady current connecting two regions with high eddy kinetic energy (Drake
462 Passage and the Brazil-Malvinas Confluence) as most of the EKE leaking from Drake Passage
463 is damped over the Malvinas Plateau. Indeed, The Malvinas Plateau is a hotspot region for
464 eddy activity dissipation (Artana et al., 2016, Figure 2a), and for local water mass properties
465 modification either through eddy mixing or through winter convection (Figure 13 a). On the
466 Malvinas Plateau, deep winter mixed layers attain on average a depth of 300 m and occasionally
467 reach 600 m. Deep mixed layers reach density values as large as 27.1 kg/m^3 , ventilating the
468 AAIW-U as observed in Piola and Gordon (1989).

469 The upper 900 m transport mean decreases from 40 Sv at 51°S to 35 Sv at 41°S indicating
470 offshore leakage along the MC path. At 51°S the upper MC volume transport (40 Sv) receives
471 a mean contribution of 3 Sv from WBB, 23 Sv from EBB and 14 Sv from SRP.

472 Computing MC transport time series at different latitudes requires care because the choice of
473 the eastern limit of the section, embedded in large EKE regions, impacts on the transport time
474 series variations. Transport time series in the upper 900 m and in the MUW layer were
475 produced considering positive (T^+) and both sign velocities (T^{+-}) to take into account the
476 difficulties associated with the open eastern boundary. The mean MUW transport is not very
477 sensitive to the different Θ/S criteria used (in the range defined by $\Theta > \Theta_0$ and $33.9 < S < S_0$ with
478 Θ_0 varying between 34.25 and 34.32) while the relative uncertainty reduces from 16% in MUW

479 (T+-) to 5% in the MUW (T+). The 900 m volume transport and the MUW transport are
480 correlated (>0.8) and show little seasonality (relative seasonal std of 2%) and no trend.
481 Differences between the upper 900 m transport and the MUW transport are modulated by the
482 occurrence of feeding events and blocking events. Indeed, waters advected during blocking
483 events (salty and warm in the upper layer) and feeding events (fresh at the surface and salty at
484 depth) are excluded from the computation of the MUW transport. The 2004 MUW transport
485 minimum (reduction of 5 Sv) was associated with a unique southward displacement of the BC
486 overshoot, blocking events at 48°S and a prolonged feeding event.

487 Synoptic transport maxima in the upper 900 m are associated either to feeding events in the
488 South or cyclonic eddies propagating north or local mesoscale activity at the Confluence
489 (Figure 13b). As cyclones with polar water do not contribute to the MUW transport, the MUW
490 maxima are not necessarily simultaneous with the upper 900 m transport maxima (Figure 13b).
491 Drastic reductions in the upper 900 m and MUW transport occurred at the Confluence and at
492 59°W during blocking events (Figure 13c). Over the 25 years, 100 blocking events and 96
493 feeding events occurred at 59°W . Blocking events at 59°W became more frequent over the last
494 decade (35 during 93-05 and 65 during 05-17). The southward displacement of the BC
495 overshoot could contribute to that increase (Figure 13c). However, the origin of the
496 perturbations leading to the blocking events remains uncertain. Backward trajectories of
497 lagrangian particles did not lead to conclusive results: tracking back anomalies in the Argentine
498 Basin is difficult because of the intense mesoscale activity. It is possible that events of transport
499 reductions as the one in 2004 will be more frequent in the future.

500 Overall the MC is a strong and steady current. The standard deviation of the transport is small
501 relative to the mean: about 10% at 44.7°S and 47°S and 20 % at 41°S near the Confluence,
502 59°W in the blocking region and 51°S on the Malvinas Plateau. In contrast, the ratio std/mean
503 of the BC transport is of the order of 57% at 37°S (Artana et al., 2019 a). The MC plays a minor

504 role in the velocity variations observed at the confluence at seasonal and interannual scales.
505 Velocity trends are small over the MC while they are large at the Brazil Malvinas Confluence
506 and the overshoot (10 cm/s/decade at the surface) as the BC migrated southward over the last
507 25 years.

508 Estimates of total volume transport provide values (70 to 45 Sv from south to north) that are in
509 agreement with the few existing estimates based on observations (Peterson, 1992; Saunders
510 and King, 1995; Maamaatuaiahutapu et al., 1998; Colin de Verdière and Ollitrault, 2016). Deep
511 Argo floats deployed in the Southern Ocean will be examined to precisely evaluate the water
512 mass characteristics and velocities at depths in GLORYS12. Furthermore, on-going efforts aim
513 at providing a new ocean reanalysis with the number of vertical levels increasing from 50 to
514 75 and assimilating deep Argo floats. These improvements will probably provide further
515 insights on deep circulation and water masses.

516 **Acknowledgments:**

517 We are grateful to the CNES (Centre National d'Etudes Spatiales) for constant support.
518 This study is a contribution to EUMETSAT/CNES DSP/OT/12-2118. Léa Poli
519 acknowledges support from Sorbonne Université and Camila Artana from a CNES Postdoc
520 Scholarship. The model outputs are available at Copernicus Marine Environment
521 Monitoring Service (CMEMS; <http://marine.copernicus.eu/>).

522

523

524

525

526

527

528

529 **References:**

530

531 Artana, C., Ferrari, R., Koenig, Z., Saraceno, M., Piola, A., & Provost, C. (2016). Malvinas
532 Current variability from Argo floats and satellite altimetry. *Journal of Geophysical Research:*
533 *Oceans*, 121, 4854–4872, <https://doi.org/10.1002/2016JC011889>

534

535 Artana, C., Ferrari, R., Koenig, Z., Sennéchaël, N., Saraceno, M., Piola, A. R., & Provost, C.
536 (2018). Malvinas Current volume transport at 41° S: A 24–year long time series consistent with
537 mooring data from 3 decades and satellite altimetry. *Journal of Geophysical Research:Oceans*,
538 <https://doi.org/10.1002/2017JC013600>

539

540 Artana, C., Lellouche, J. M., Park, Y. H., Garric, G., Koenig, Z., Sennéchaël, N., et al. (2018).
541 Fronts of the Malvinas Current System: surface and subsurface expressions revealed by
542 satellite altimetry, Argo floats, and Mercator operational model outputs. *Journal of*
543 *Geophysical Research: Oceans*, <https://doi.org/10.1029/2018JC013887>

544

545 Artana, C., Lellouche, J.-M., Sennéchaël, N., & Provost, C. (2018). The open-ocean side of the
546 Malvinas Current in Argo float data and 25 years of reanalyses from Mercator operational
547 system. *Journal of Geophysical Research: Oceans*, 123, 8489–8507, [https://doi.org/10.1029/](https://doi.org/10.1029/2018JC014528)
548 [2018JC014528](https://doi.org/10.1029/2018JC014528).

549

550 Artana, C., Provost, C., Lellouche, J.-M., Rio, M.-H., Ferrari, R., & Sennéchaël, N. (2019).
551 The Malvinas Current at the Confluence with the Brazil Current: Inferences from 25 years of
552 Mercator Ocean reanalysis. *Journal of Geophysical Research: Oceans*, 124,
553 <https://doi.org/10.1029/2019JC015289>

554

555 Artana, C., Ferrari, R., Bricaud, C., Lellouche, J.-M., Garric, G., Sennéchaël, N., Lee, J.-H.,
556 Park, Y.-H. & Provost, C. (2019). Twenty-five years of Mercator ocean reanalysis GLORYS12
557 at Drake Passage: velocity assessment and total volume transport. *Journal of Advances in*
558 *Space Research*, <https://doi.org/10.1016/j.asr.2019.11.033>

559

560 Barré, N., Provost, C., & Saraceno, M. (2006). Spatial and temporal scales of the Brazil-
561 Malvinas Confluence documented by simultaneous MODIS Aqua 1.1-km resolution SST and
562 color images. *Journal of Advances in Space Research*, 37(4), 770–
563 786,<https://doi.org/10.1016/j.asr.2005.09.026>

564

565 Böning, C. W., Dispert, A., Visbeck, M., Rintoul, S. R., & Schwarzkopf, F. U. (2008). The
566 response of the Antarctic Circumpolar Current to recent climate change. *Nature Geoscience*,
567 1(12), 864–869, <https://doi.org/10.1038/ngeo362>

568

569 Boyer Montegut, C., G. Madec, A. S. Fischer, A. Lazar, & D. Iudicone (2004). Mixed layer
570 depth over the global ocean: An examination of profile data and a profile-based climatology,
571 *Journal of Geophysical Research*, 109, C12003, <https://doi.org/10.1029/2004JC002378>.

572
573
574
575
576
577
578
579
580
581
582
583
584
585
586
587
588

589
590
591

592
593
594
595
596
597
598
599
600
601
602
603
604
605
606
607
608
609
610
611
612
613
614
615
616
617

Cabanes, C., Grouazel, A., Schuckmann, K. V., Hamon, M., Turpin, V., Coatanoan, C., et al. (2013). The CORA dataset: Validation and diagnostics of in-situ ocean temperature and salinity measurements. *Ocean Science*, 9(1), 1–18, <https://doi.org/10.5194/os-9-1-2013>

Close, S. E., Garabato, A. C. N., Mcdonagh, E. L., King, B. A., Biuw, M., & Boehme, L. (2013). Control of mode and intermediate water mass properties in Drake passage by the Amundsen sea low. *Journal of Climate*, 26(14), 5102–5123, <https://doi.org/10.1175/JCLI-D-18-0205.1>

Colin de Verdière, A., and M.Ollitrault, 2016: Direct determination of the world ocean barotropic circulation. *Journal of Physical Oceanography* , 46, 255–273, <https://doi:10.1175/JPO-D-15-0046.1>.

Frey, D. I., Piola, A. R., Krechik, V. A., Fofanov, D. V., Morozov, E. G., Silvestrova, K. P., et al. (2021). Direct measurements of the Malvinas Current velocity structure. *Journal of Geophysical Research: Oceans*, 126, e2020JC016727. <https://doi.org/10.1029/2020JC016727>

Gordon, A. L., & C. L. Greengrove (1986). Geostrophic circulation of the Brazil-Falkland Confluence, *Deep Sea Research, Part A*, 33, 573 – 585, [https://doi.org/10.1016/0198-0149\(86\)90054-3](https://doi.org/10.1016/0198-0149(86)90054-3)

Gordon, A. L., Weiss, R., Smethie, W., & Warner, M. (1992). Thermocline and intermediate water communication between the South Atlantic and Indian Oceans. *Journal of Geophysical Research*, 97, 7223–7240, <https://doi.org/10.1029/92JC00485>

Lellouche, J.-M., Greiner, E., Le Galloudec, O., Garric, G., Regnier, C., Drevillon, M., et al. (2018). Recent updates on the Copernicus Marine Service global ocean monitoring and forecasting real-time 1/12° high resolution system. *Ocean Science Discussions*. <https://doi.org/10.5194/os-2018-15>

Lellouche, J.-M., Le Galloudec, O., Drevillon, M., Regnier, C., Greiner, E., Garric, G., et al. (2013). Evaluation of real time and future global monitoring and forecasting systems at Mercator Ocean. *Ocean Science Discussions*, 9, 1123–1185, <https://doi.org/10.5194/osd-9-1123-2012>

Maamaatuaiahutapu, K., Garçon, V., Provost, C., Boulahdid, M., & Bianchi, A. A. (1994). Spring and winter water mass composition in the Brazil-Malvinas Confluence. *Journal of Marine Research*, 52, 397–426, <https://doi.org/10.1357/0022240943077064>

Maamaatuaiahutapu, K., V. Garçon, C. Provost, & H. Mercier (1998). Transports of the Brazil and Malvinas Currents at their confluence, *Journal of Marine Research*, 56, 417–438, <https://doi.org/10.1357/002224098321822366>

Mulet S., M.-H. Rio, H. Etienne, C. Artana, M. Cancet, G. Dibarboure, H. Feng, R. Husson, N. Picot, C. Provost, & P. T. Strub (2020). The new CNES-CLS18 Global Mean Dynamic Topography. *Ocean Science*, MS <https://doi.org/10.5194/os-2020-117>

618 Naveira Garabato, A. C., Jullion, L., Stevens, D. P., Heywood, K. J., & King, B. A. (2009).
619 Variability of subantarctic mode water and Antarctic Intermediate Water in the Drake Passage
620 during the late-twentieth and early-twenty-first centuries. *Journal of Climate*, 22(13),
621 3661–3688, <https://doi.org/10.1175/2009JCLI2621.1>
622

623 Paniagua, G., Saraceno, M., Piola, A., Provost, C., Guerrero, R., Ferrari, R., et al. (2018).
624 Dynamics of the Malvinas Current at 41°S: First assessment of temperature and salinity
625 temporal variability. *Journal of Geophysical Research: Oceans*, [https://doi.org/10.1029/](https://doi.org/10.1029/2017JC013666)
626 2017JC013666

627 Peterson, R. G., & Whitworth, T. (1989). The subantarctic and polar fronts in relation to deep
628 water masses through the southwestern Atlantic. *Journal of Geophysical Research*, 94(C8),
629 10,817–10,838, <https://doi.org/10.1029/JC094iC08p10817>

630 Peterson, R. G. (1992), The boundary currents in the western Argentine Basin, *Deep Sea*
631 *Research. Part A*, 39(3-4), 623–644. [https://doi.org/10.1016/0198-0149\(92\)90092-8](https://doi.org/10.1016/0198-0149(92)90092-8)
632

633 Piola A. & Gordon A.L. (1989). Intermediate waters in the southwest South Atlantic. *Deep-*
634 *Sea Research*, Vol. 36, No. 1, pp. 1-16, 1989, [https://doi.org/10.1016/0198-0149\(89\)90015-0](https://doi.org/10.1016/0198-0149(89)90015-0)
635

636 Piola, A. R., Franco, B. C., Palma, E. D., & Saraceno, M. (2013). Multiple jets in the Malvinas
637 Current. *Journal of Geophysical Research: Oceans*, 118, 2107–2117,
638 <https://doi.org/10.1002/jgrc.20170>
639

640 Poli, L., Artana, C., Provost, C., Sirven, J., Sennéchaël, N., Cuypers, Y., & Lellouche, J.-M.
641 (2020). Anatomy of subinertial waves along the Patagonian shelf break in a 1/12° global
642 operational model. *Journal of Geophysical Research: Oceans*, 125, e2020JC016549, [https://](https://doi.org/10.1029/2020JC016549)
643 doi.org/10.1029/2020JC016549
644

645 Provost, C., Gana, S., Garçon, V., Maamaatuaiahutapu, K., & England, M. (1995).
646 Hydrographic conditions during austral summer 1990 in the Brazil/Malvinas Confluence
647 region. *Journal of Geophysical Research*, 100(C6), 10655–10682,
648 <https://doi.org/10.1029/94JC02864>
649

650 Pujol, M.-I., Faugère, Y., Taburet, G., Dupuy, S., Pelloquin, C., Ablain, M., & Picot, N. (2016).
651 DUACS DT2014: The new multi-mission altimeter data set reprocessed over 20 years. *Ocean*
652 *Science*, 12(5), 1067–1090., <https://doi.org/10.5194/os-12-1067-2016>
653

654 Purich, A., England, M. H., Cai, W., Sullivan, A., & Durack, P. J. (2018). Impacts of broad-
655 scale surface freshening of the Southern Ocean in a coupled climate model. *Journal of Climate*,
656 31(7), 2613–2632, <https://doi.org/10.1175/JCLI-D-17-0092.1>
657

658 Romero, S. I., Piola, A. R., Charo, M., & Garcia, C. A. E. (2006). Chlorophyll-a variability off
659 Patagonia based on SeaWiFS data. *Journal Geophysical Research*, 111, C05021.
660 <https://doi.org/10.1029/2005JC003244>

661 Saraceno M., Provost C., Piola A., Guerrero R., Ferrari R., Paniagua G. F., Lago L. S., &
662 Artana C. (2020). Malvinas Current 2015-2017: Mooring velocities. SEANOE,
663 <https://doi.org/10.17882/76617>
664

665 Saunders, P. M. & B. A. King. (1995). Bottom currents derived from a shipborne ADCP on
666 WOCE cruise A11 in the South Atlantic. *Journal of Physical Oceanography*, 25, 329–347,
667 [https://doi.org/10.1175/1520-0485\(1995\)025](https://doi.org/10.1175/1520-0485(1995)025).
668

669 Smith, W. H. F., & Sandwell, D. T. (1994). Bathymetric prediction from dense satellite
670 altimetry and sparse shipboard bathymetry. *Journal of Geophysical Research*, 99, 21 803–21
671 824. <https://doi.org/10.1029/94JB00988>
672

673 Spadone, A., & Provost, C. (2009). Variations in the Malvinas Current volume transport since
674 October 1992. *Journal of Geophysical Research*, 114, C02002,
675 <https://doi.org/10.1029/2008JC004882>
676

677 Szekeley, T., Gourrion, J., Pouliquen, S., & Reverdin, G. (2016). CORA, Coriolis, Ocean
678 Dataset for Reanalysis. SEANOE, <https://doi.org/10.1029/2008JC05248>
679

680 Valla, D., & Piola, A. R. (2015). Evidence of upwelling events at the northern Patagonian shelf
681 break. *Journal of Geophysical Research: Oceans*, 120, 7635–7656.
682 <https://doi.org/10.1002/2015JC011002>
683

684 Vivier, F., & Provost, C. (1999a). Direct velocity measurements in the Malvinas Current.
685 *Journal of Geophysical Research*, 104, 21083–21104. <https://doi.org/10.1029/1999JC900163>
686

687 Vivier, F., & Provost, C. (1999b). Volume transport of the Malvinas Current: Can the flow be
688 monitored by TOPEX/Poseidon? *Journal of Geophysical Research*, 104, 21105–21122.
689 <https://doi.org/10.1029/1999JC900056>
690
691
692
693
694
695
696
697
698
699
700
701
702
703
704

705 **Figure Captions:**

706 **Figure 1:** a) Bottom topography of the Southwestern Atlantic and Drake Passage (in meters)
707 from Smith and Sandwell (1994). The main passages through North Scotia Ridge are indicated:
708 West of Burwood Bank (WBB), East of Burwood Bank (EBB), and Shag Rocks Passage (SRP).
709 The mean location of the Antarctic Circumpolar Current fronts is schematized: Subantarctic
710 Front (SAF-N and SAF-M, blue dashed and solid lines), Polar Front (PF-N and PF-M in yellow
711 solid and dashed lines), and Southern ACC Front (SACFF, in green). The mean position of the
712 Brazil Current Front (BCF) is indicated in red. b) mean surface velocities from 1993 to 2017
713 (in cm/s) from the ocean reanalysis (GLORYS12) documented in this study. c) Square root of
714 eddy kinetic energy over 25 years (in cm/s) from GLROYS12. In b and c the 300, 500 and
715 1500 m isobaths are indicated with thick black contours and the 6,000, 5,000, 3,000, 2,000 with
716 gray contours. Five sections crossing the MC at 41°S (red), 44.7°S (blue), 47°S (orange),
717 59°W(green) and 51°S (purple) and three sections at North Scotia Ridge, WBB, EBB and SRP
718 (magenta) are indicated.

719

720 **Figure 2:** Schematics of physical processes in the MC based on previous studies. a) Grey
721 shading represents dissipation over the Malvinas Pateau of the mesoscale activity leaking
722 through North Scotia Ridge (Artana et al., 2016). Trapped waves (locally wind forced and
723 remotely forced) propagating along the Patagonian slope are schematized in blue (Poli et al.,
724 2020). b) Blocking events in red: anticyclonic anomalies cut the MC from the Antarctic
725 Circumpolar Current at 49°S; the MC does not collapse as a recirculation cell is established
726 (Artana et al., 2016 and 2018c). Feeding events in blue: waters from the South of the Polar
727 Front are injected into the MC and recirculate between the MC and Malvinas Return Flow
728 (Artana et al., 2018c). c) Maxima and minima of the MC transport at 41°S are associated with
729 eddies coming from the Argentine Basin: Transport maximum cases (in blue) are associated

730 with cyclonic eddies detached from the PF and transport minimum cases (in red) with
731 southward displacement of the Subantarctic Front due to large anticyclonic anomalies from the
732 Brazil Current (Artana et al., 2018a).

733

734 **Figure 3:** a) Bathymetry gradient (m/km). Dashed lines indicate the 300, 500 and 1500 m
735 isobaths. (b) Mean along-slope surface velocities in cm/s along five sections crossing the MC
736 at 41°S (red), 44.7°S (blue), 47°S (orange), 59°W (green) and 51°S (purple) (indicated in a).
737 Shaded areas correspond to the velocity std. X-axis is distance in km from isobath 100 m. (c)
738 Bathymetry along the same sections (same color code). Y-axis is depth in meters. Solid and
739 dashed vertical lines indicate the location of maximum velocities of the offshore (SAF-M) and
740 inshore (SAF-N) jets.

741

742 **Figure 4:** Surface velocity anomalies over 25 years (in cm/s) in February (a) and August (b).
743 The mean position of the Subantarctic Front (Sea Surface Height = -5 cm) and Brazil Current
744 Front (Sea Surface Height = 30 cm) are indicated in black contours. c-d) Significant linear
745 trends (above the 95% confidence level) in surface velocity (cm/s/decade) and EKE
746 ($\text{cm}^2/\text{s}^2/\text{decade}$) computed over 25 years (1993-2017). The black contour delineates points
747 where the 25-year trend is larger than the std. Isobaths as in figure 2. Five sections crossing the
748 MC at 41°S (red), 44°S (blue), 47°S (orange), 59°W (green) and 51°S (purple) three sections
749 at North Scotia Ridge (in magenta) are indicated.

750

751 **Figure 5:** Mean transport stream functions computed between surface and 900 m depth over
752 25 years (a), over the 25 months of February (b) and August (c), over full year 2015 (d) and
753 full year 2003 (e). Streamlines are plotted every 5 Sv. Background is mean volume transport
754 (in Sv) in each model grid (transport density). Five sections crossing the MC at 41°S (red),

755 44°S (blue), 47°S (orange), 59°W (green) and 51°S (purple) and three sections at North Scotia
756 Ridge (in magenta) are indicated.

757

758 **Figure 6:** (a-d) Mean and (e-h) std of potential temperature (°C), salinity (psu), density (kg/m³)
759 and along slope velocities from GLORYS12 (1993-2017) along the Patagonian slope at 51°S
760 (purple section in j). X-axis in km from the 100 m isobath and Y-axis is depth in m. The 2.5
761 °C isotherm and 34.25 psu isohaline are indicated in red, the 27.00, 27.14, 27.29, 27.35 kg/m³
762 isopycnal in dashed white. i) Corresponding mean Θ -S diagram. The vertical rectangle marks
763 34.25 and 34.32 psu values and the horizontal rectangle the 2.5 and 2.7°C values. j) Mean Sea
764 Surface Height (in cm) over 25 years. The SAF-N/SAF-M and PF-N/PF-M are indicated in
765 solid/dashed blue and red lines respectively.

766

767 **Figure 7:** a) Mean thickness (in m) of MUW layer (waters with $\Theta_{\text{mean}} > 2.5$ °C and $33.9 < S_{\text{mean}}$
768 < 34.32 psu) b) Mean depth (in m) of the upper boundary of the MUW layer c) Presence
769 probability of MUW over upper 900m. 100% means that these waters occupy the whole upper
770 900 m all the time. Black solid and dashed contour indicates the position of the Subantarctic
771 Front and Polar Front and the red contour the position of the Subtropical Front.

772

773 **Figure 8:** Mean (a and c) and maximum (b and d) mixed layer depth (in m) and surface
774 potential density in August. Grey colors indicate regions where the MLDs reach the bottom e)
775 Mixed layer depth (purple in m) and potential density (in kg/m³) time series above the Malvinas
776 Plateau at the blue point indicated in a-c.

777

778 **Figure 9:** a): Sea Surface Height map of 2 January 2011. The position of the SAF-M/SAF-N
779 and PF-N/PF-M are indicated in blue and red. The 500, 1000, 1500, 2000 and 2500 m isobaths

780 are indicated in grey. b,c and d): Salinity, Temperature and along slope velocities over the 51°S
781 section indicated in purple in Figure a. The 2.5°C and 2.7°C isotherms and the 34.32 psu and
782 34.25 psu isohaline are indicated with dashed red contour. The MLD is indicated with a pink
783 contour. e) Θ -S diagram from January 2011 over the 51°S section indicated in grey in a) The
784 vertical rectangle marks 34.25 and 34.32 psu values and the horizontal rectangle the 2.5 and
785 2.7°C values. In colors selected profiles from 2 January. The location of each profile is
786 indicated with colored diamonds in a (f-j) same for August 2011. The selected profiles are from
787 the 31 August 2011.

788

789 **Figure 10:** a) Stream function of the mean volume transport associated to the MUW layer ($\Theta > 2.5$
790 °C and $33.9 < S < 34.25$ psu). Background is mean volume transport in each model grid (in Sv) and
791 isolines are plotted every 5 Sv. Monthly (c) and yearly (c) averages of MUW volume transport
792 (in Sv) along in the MC.

793

794 **Figure 11:** Volume transport time series across the MC at (a) 44°S and (b) 47°S. Dark-colored
795 timeseries correspond to MUW volume transport and light-colored time series to the volume
796 transport integrated over the upper 900 m. Difference between the two transport time series at
797 44°S in blue (c) and 47°S in orange(d). Superimposed in black is the time series of potential
798 density at 541 m averaged over the yellow box in Figure 12 d. Densities larger than the std in
799 blue indicate feeding while densities lower than the std in red indicate blocking events (Artana
800 et al., 2018c).

801

802 **Figure 12:** a): Mean Sea Level Pressure contours averaged over 2004 (in red) and over the 25
803 years (in blue). b and d): Mean salinity at the surface and 541 m over 2004. The cyan and red
804 contour represent the mean position of the 33.9 and 34.25 psu isohalines. c and e): Salinity

805 anomaly at the surface and 541 m over 2004. Indicated are five sections along the MC and
806 three sections across North Scotia Ridge and a yellow box in d) over which spatially averaged
807 time series of potential density are computed (shown in Figure 11 c and d).

808

809 **Figure 13:** Schematics of MC transports and physical processes. a) The mean and std of the
810 upper 900 m transports (T+ 900 m) and the MUW transports (T+ MUW) are indicated in red
811 and green boxes. The Malvinas Plateau is home to active eddy mixing, eddy dissipation and
812 deep winter mixed layers occasionally reaching 600 m depth (yellow). b) Synoptic transport
813 maxima correspond either to polar front meanders or to cyclones. c) Synoptic transport minima
814 are associated with anticyclones. The southward migration of the Brazil Current overshoot (red
815 arrow) led to an increase of mesoscale activity south of 44°S

816

817

818

819

820

821

822

823

824

825

826

827

828

829

830 **Tables caption:**

831

832 **Table 1:** Statistics of the upper 900 m volume transport computed considering only positive
833 (T+) and all velocities (T+-) velocities across 5 sections crossing the MC at 41°S, 44°S, 47°S,
834 59°W and 51°S and 3 sections at North Scotia Ridge : at EBB, WBB and SRP (location
835 indicated in Figure 1c). The correlation coefficient (r) between transport time series computed
836 from T+ and T+/- is reported in the last column.

837

838 **Table 2:** Correlations between the transport time series at different latitudes. In each box, the
839 first line corresponds to the volume transport in the upper 900 m, the second line to the MUW
840 volume transport. Both transport time series were computed only considering positive
841 velocities.

842

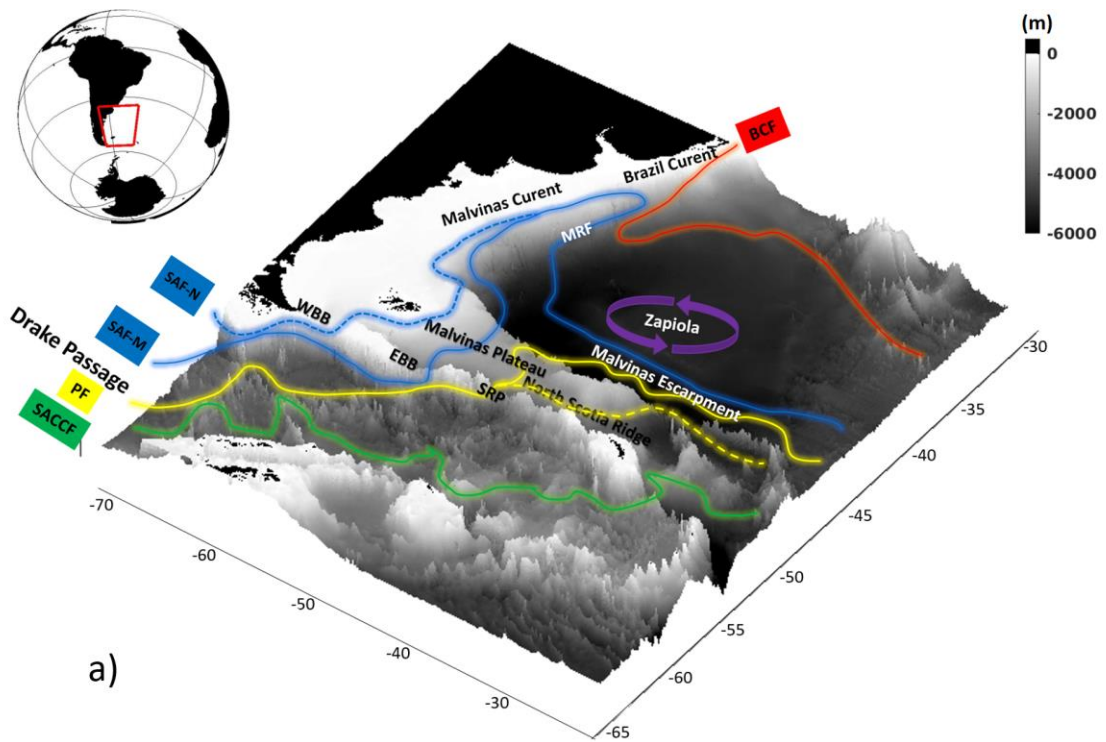
843 **Table 3:** statistics for MUW transport computed considering positive (T+) and both sign
844 velocities (T+-) across 5 sections crossing the MC at 41°S, 44°S, 47°S, 59°W and 51°S and 3
845 sections at North Scotia Ridge: at EBB, WBB and SRP (location indicated in Figure 1c). The
846 correlation coefficient (r) between transport time series computed from T+ and T+/- is reported
847 in the last column.

848

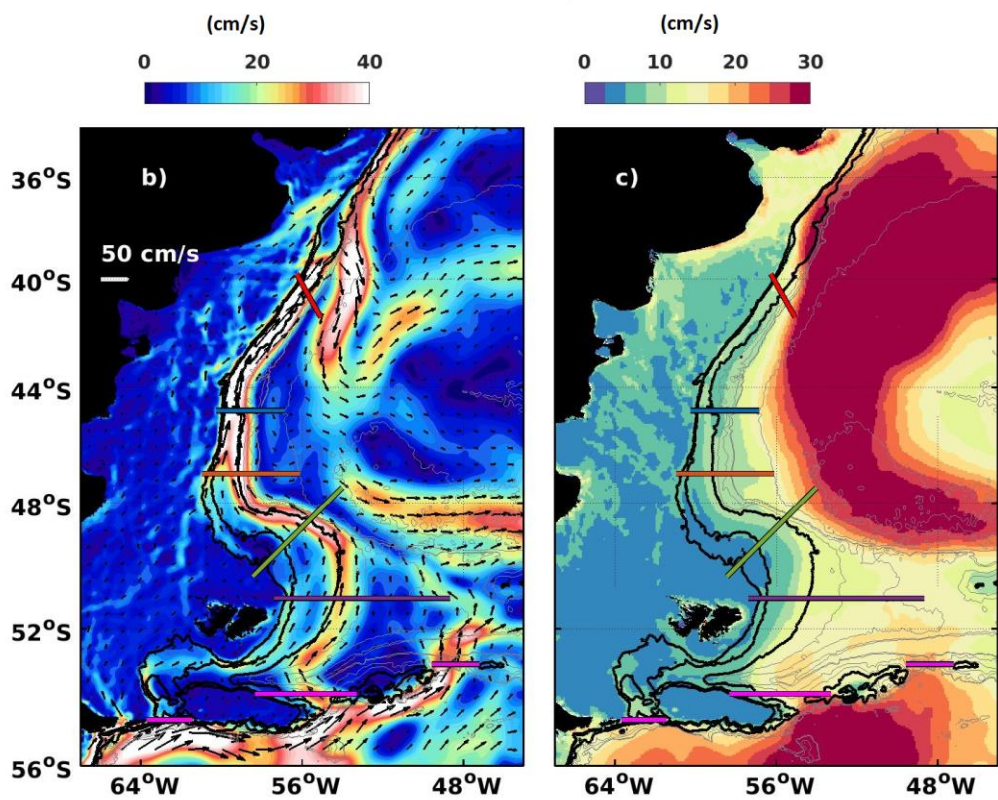
849

850

851

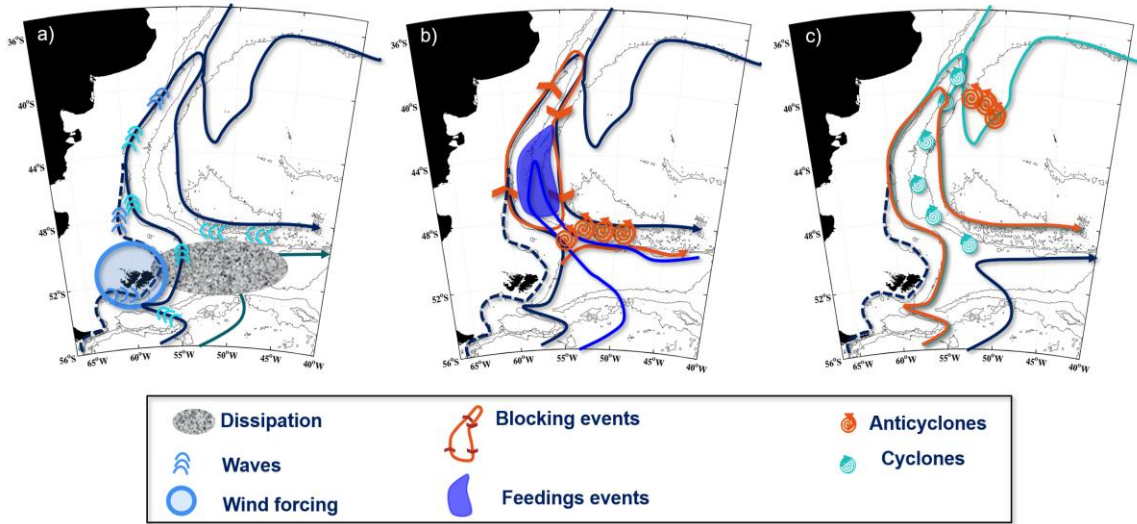


a)

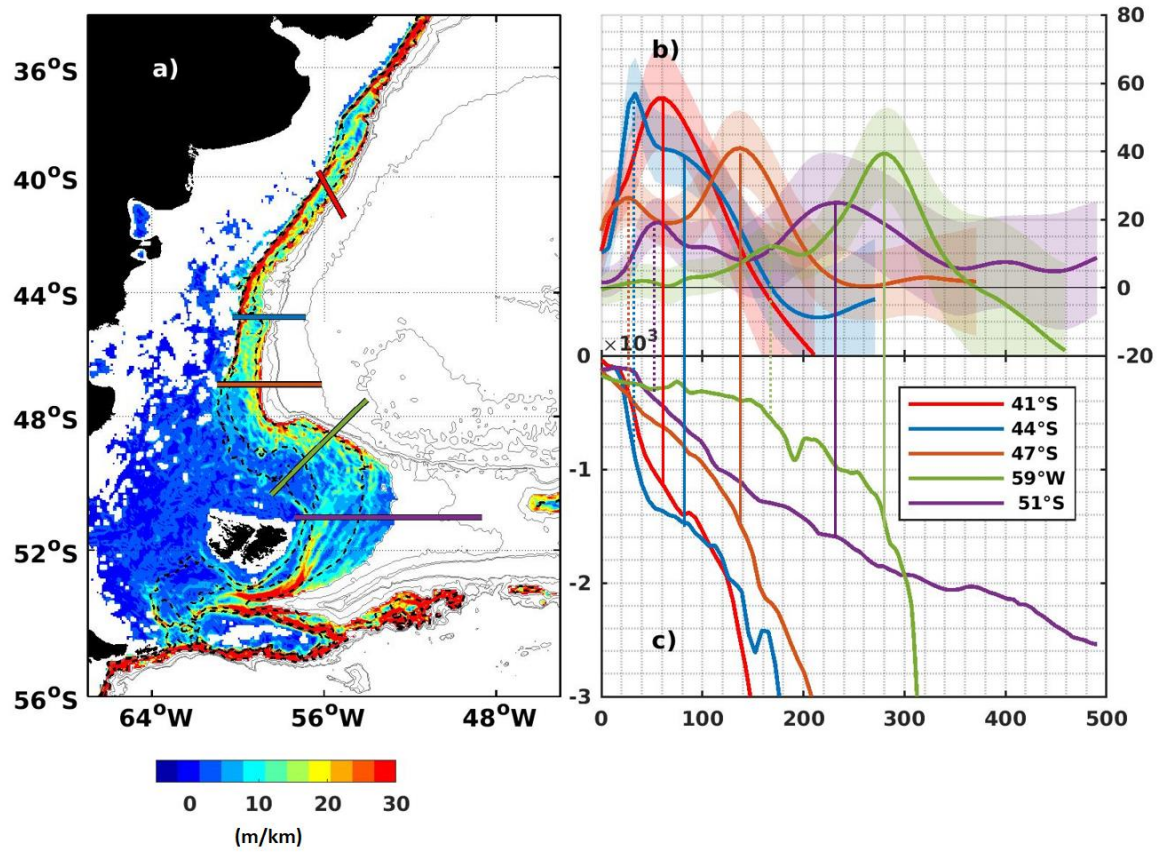


852

853 Figure 1

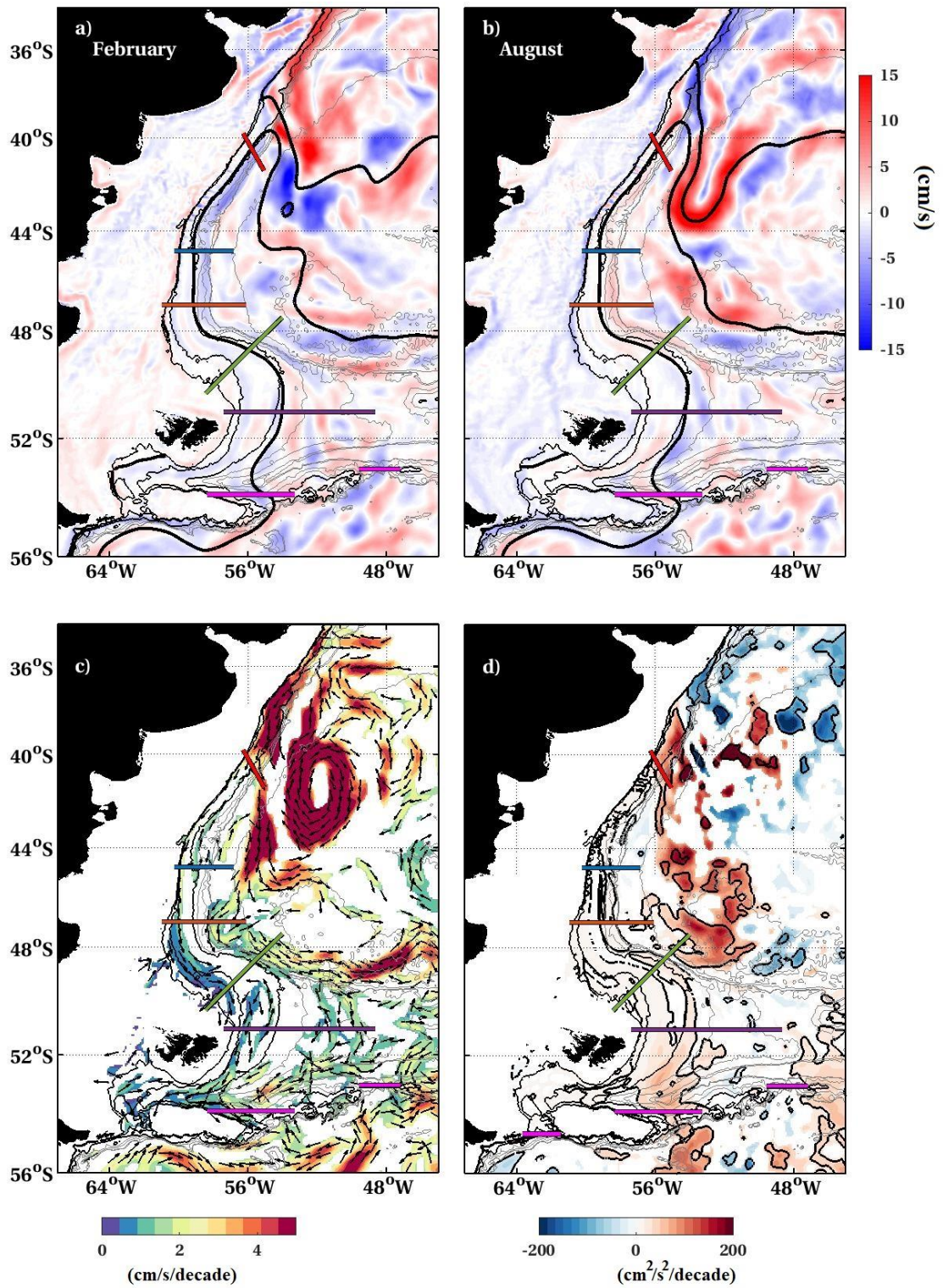


854
 855 **Figure 2**
 856
 857
 858
 859
 860
 861
 862
 863
 864
 865
 866
 867
 868
 869
 870
 871
 872
 873
 874



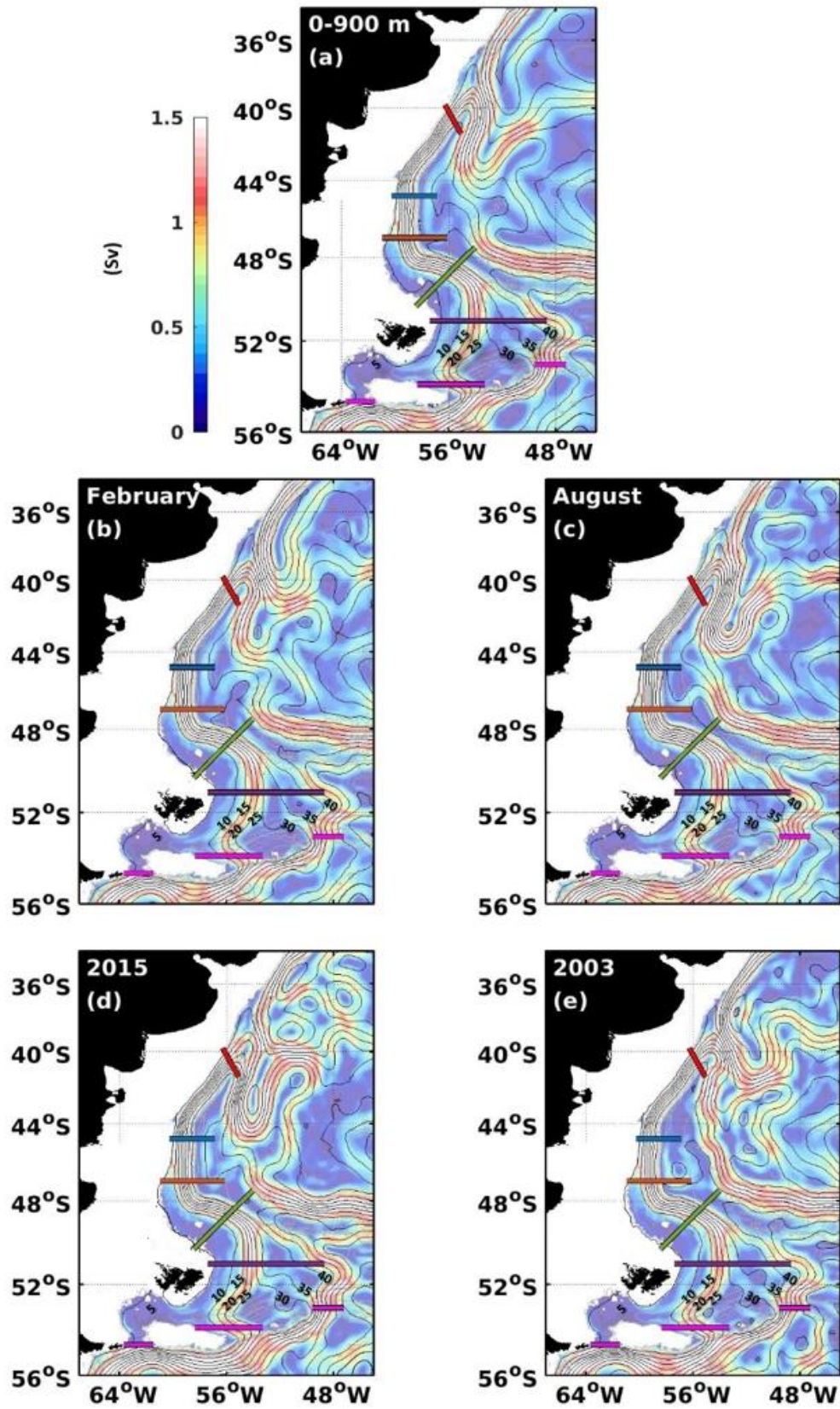
875
 876
 877
 878
 879
 880
 881
 882
 883
 884

Figure 3



885
886
887
888
889

Figure 4



890
891 Figure 5

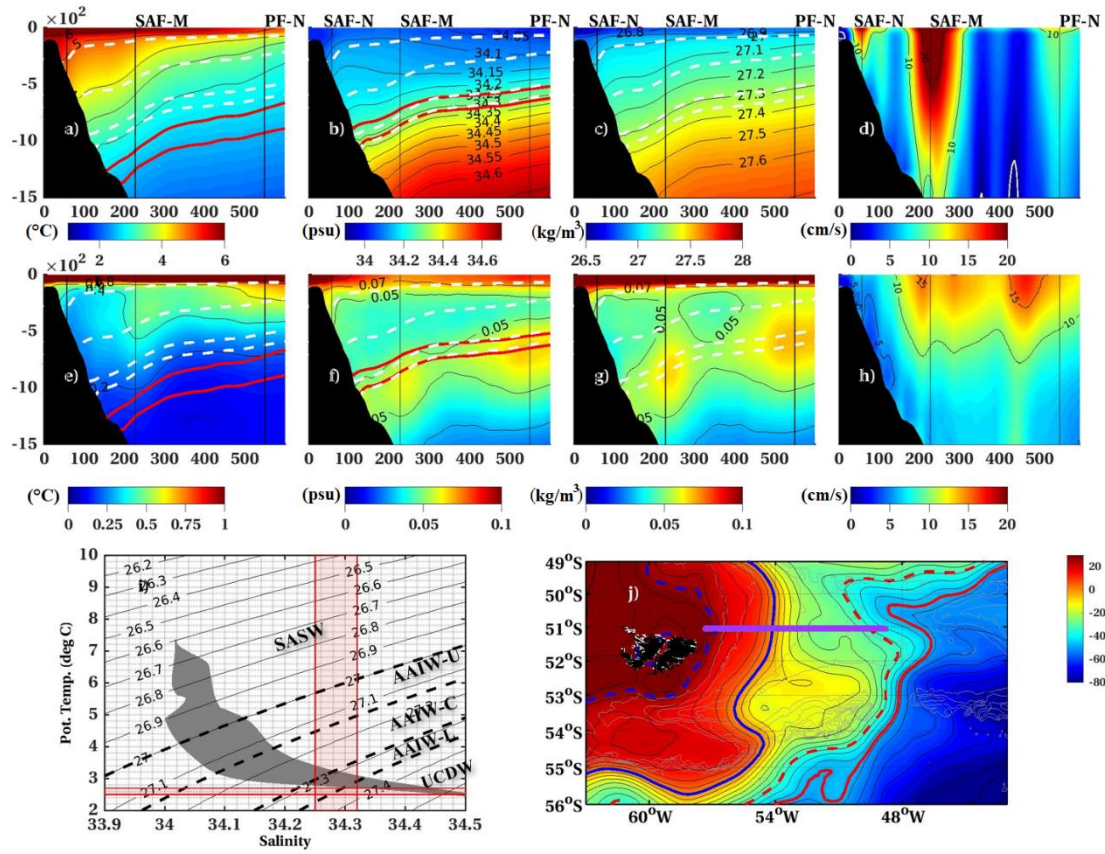
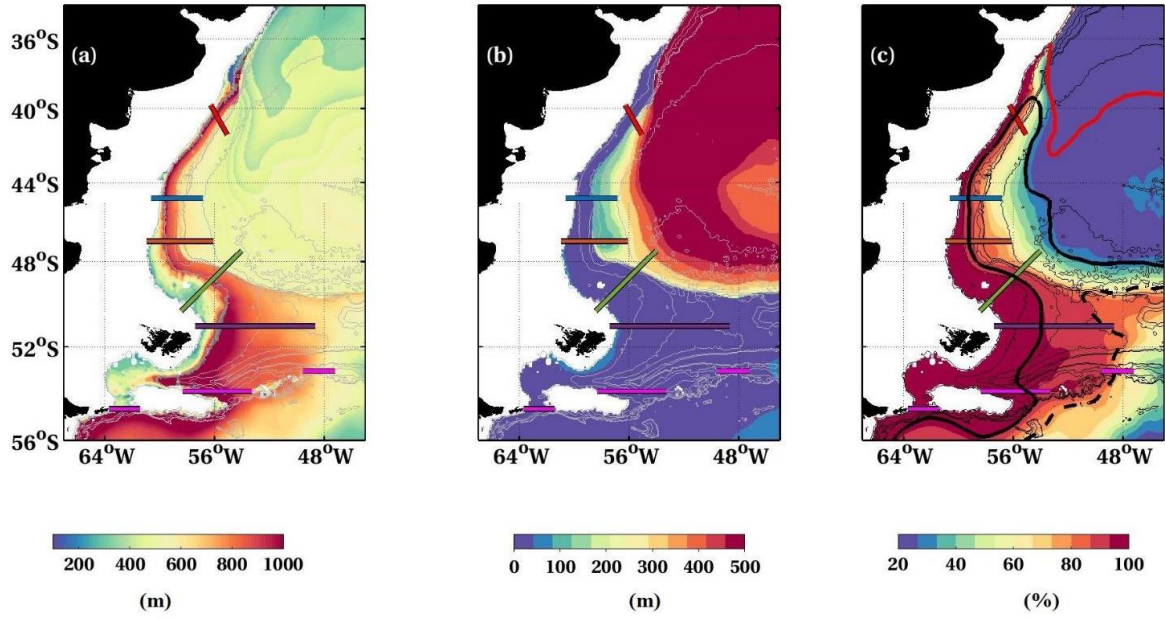


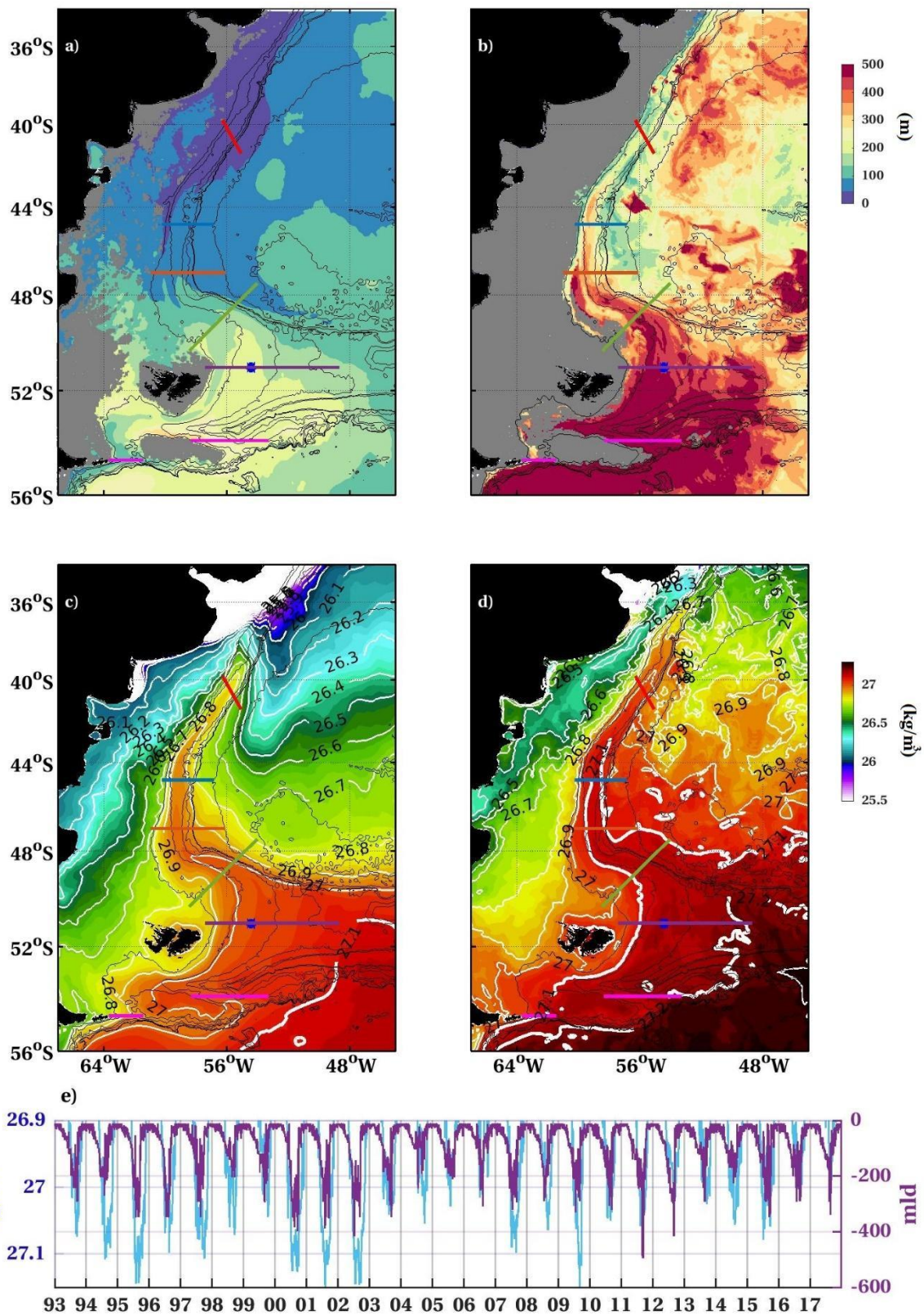
Figure 6

892
 893
 894
 895
 896
 897
 898
 899
 900
 901
 902
 903
 904

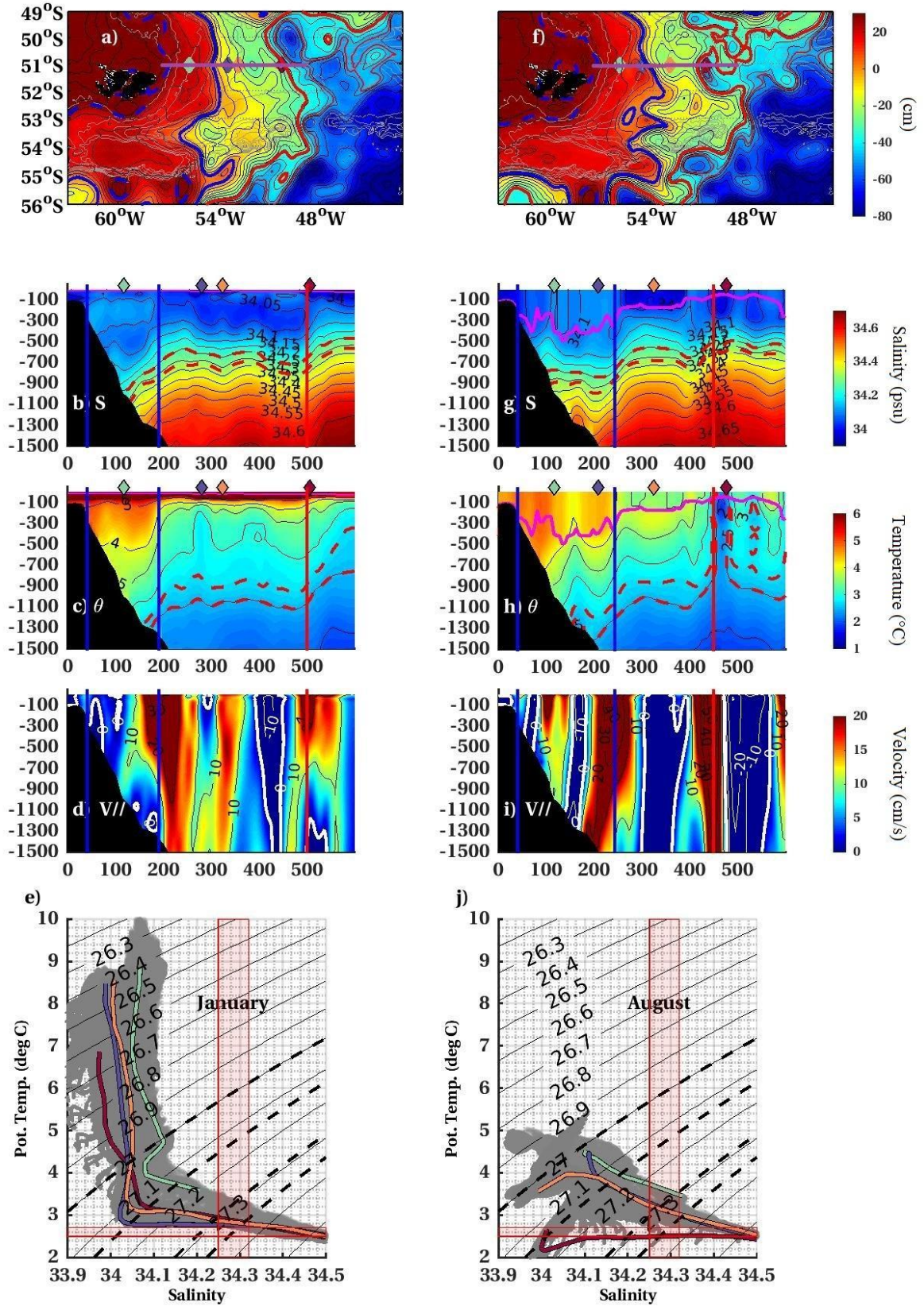


905
 906
 907
 908
 909
 910
 911
 912
 913

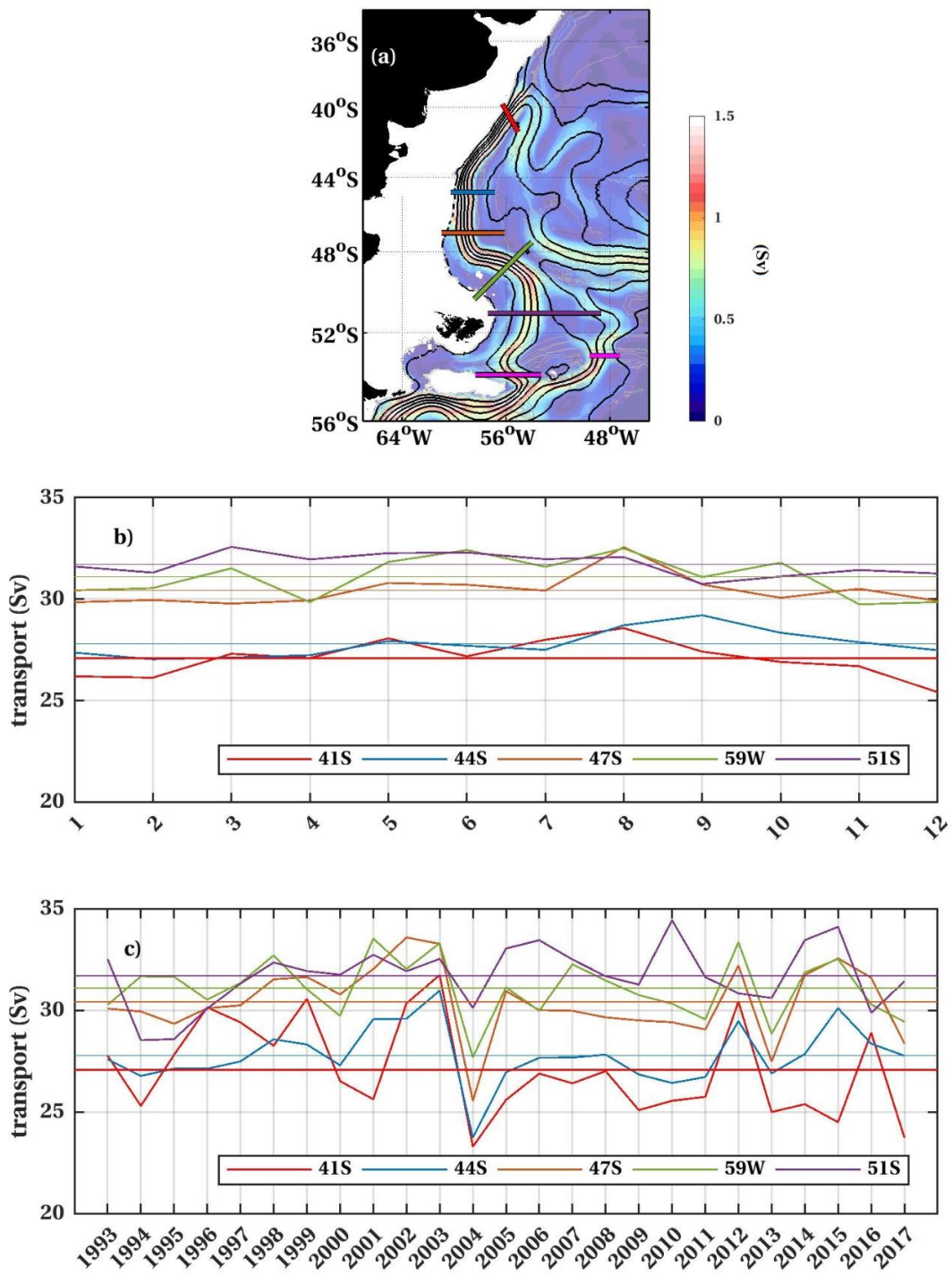
Figure 7



914
915 **Figure 8**

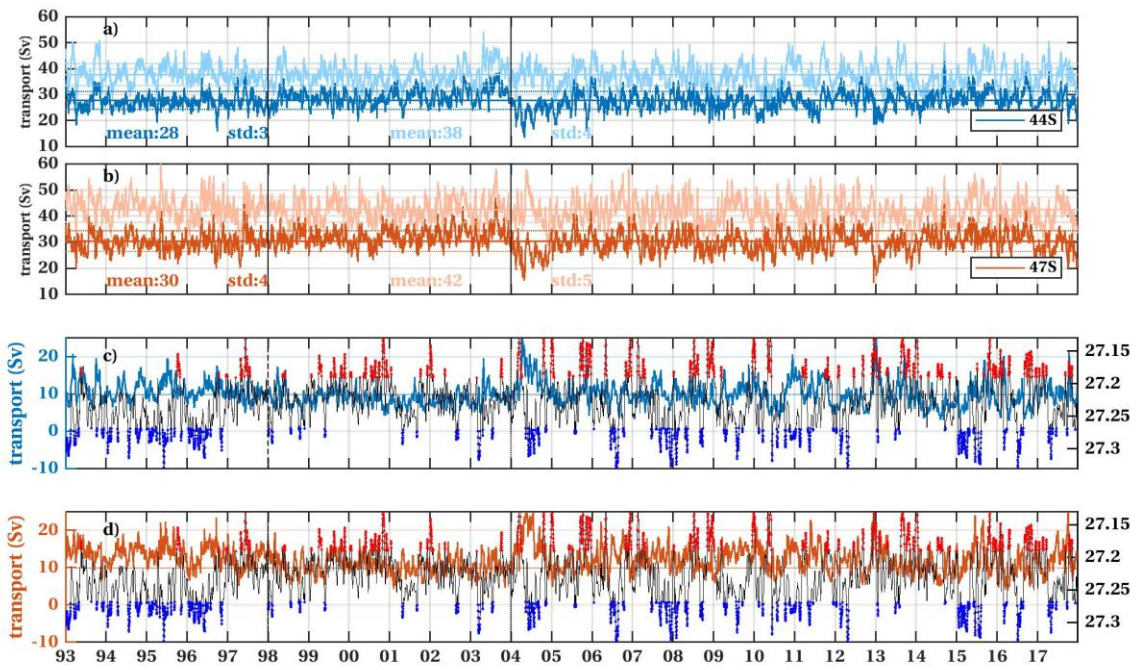


916
 917 **Figure 9**
 918

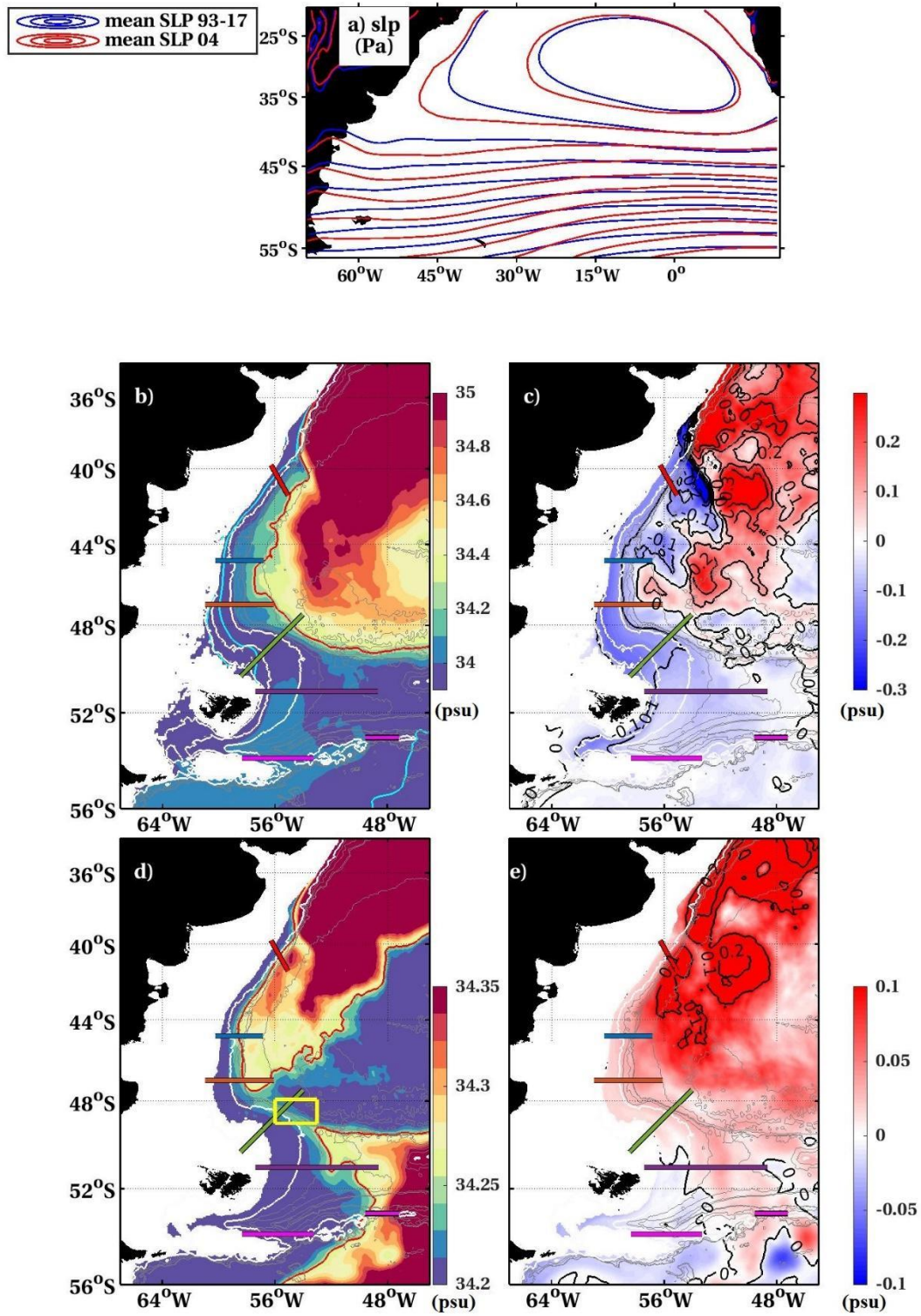


919
 920
 921
 922
 923

Figure 10

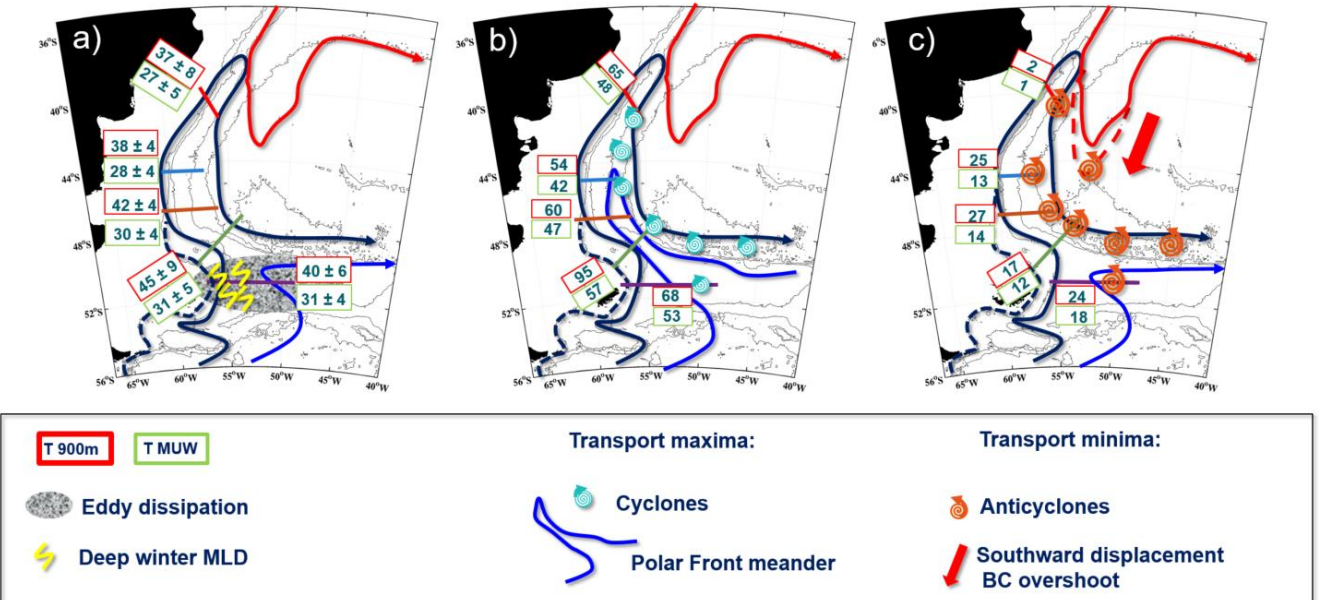


924
 925 **Figure 11**
 926



927
 928
 929
 930
 931

Figure 12



932

933

934 Figure 13

935

936

937

938

939

940

941

942

943

944

945

946

947

948

949

950 **Tables:**

951 **Table1:**

952

section	Upper 900 m volume transport (T+) /(T+-)						
	mean (Sv)	std (Sv)	Mean seasonal range (Sv)	Interannual range (Sv)	Synoptic max (Sv)	Synoptic min (Sv)	r
41°S	37/30	8/13	5/7	14/30	65/65	2/-25	0.86
44.7°S	38/29	4/8	3/4	6/16	54/52	25/-7	0.62
47°S	42/37	4/6	5/5	5/8	60/58	27/13	0.80
59°W	45/35	9/15	5/8	9/13	95/95	17/-20	0.85
51°S	40/34	6/9	3/4	8/8	68/57	24/8	0.73
EBB	23/20	6/6	4/4	7/6	57/55	7/4	0.86
SRP	31/30	7/7	5/5	9/10	55/55	6/0	0.91
WBB	3/1	1/1	1/1	1/1	7/6	0/-1	0.97
EBB +SRP+ WBB	57/51	8/8	7/4	9/7	93/90	33/22	0.92

953

954

955

956

957

958

959

960

961

962

963

964

965

966

967

968

969

970

971

972

973

974 **Table 2:**
975

	41°S	44°S	47°S	59°W	51°S
41°S		0.13 0.59	0.15 0.27	0.11 0.16	0.12 0.17
44.7°S			0.30 0.54	0.16 0.30	NS 0.20
47°S				0.37 0.44	0.12 0.21
59°W					0.14 0.18

976
977
978
979
980
981
982
983
984
985
986
987
988
989
990
991
992
993
994
995
996
997
998
999
1000
1001
1002
1003
1004
1005
1006
1007
1008
1009
1010
1011

1012 Table 3
 1013
 1014

section	Volume transports T+/T+-				
	mean (Sv)	std (Sv)	max (Sv)	min (Sv)	r
41°S	27/23	5/7	48/48	1/-6	0.86
44.7°S	28/23	3/5	42/39	13/-0.9	0.71
47°S	30/27	4/4	47/46	14/7	0.87
59°W	31/25	5/8	57/57	12/-3	0.84
51°S	31/27	4/4	53/44	18/7	0.74
EBB	20/17	6/4	41/35	6/4	0.90
SRP	15/15	4/6	40/40	0/4	0.99
WBB	2/1	0.9/0.7	6/5	0.3/-1	0.87
EBB +SRP+WBB	38/34	7/6	63/59	17/9	0.94

1015
 1016
 1017
 1018
 1019
 1020
 1021
 1022
 1023
 1024
 1025
 1026
 1027
 1028
 1029
 1030
 1031
 1032